DTU Library

A comprehensive analysis of time-dependent performance of a solar chimney power plant equipped with a thermal energy storage system

Arefian, Amir; Hosseini-Abardeh, Reza; Rahimi-Larki, Mohsen; Torkfar, Arman; Sarlak, Hamid

Published in:
Renewable and Sustainable Energy Reviews

Link to article, DOI:
10.1016/j.rser.2023.114051

Publication date:
2024

Document Version
Publisher's PDF, also known as Version of record

Renewable and Sustainable Energy Reviews 189 (2024) 114051

Contents lists available at ScienceDirect

Renewable and Sustainable Energy Reviews

journal homepage: www.elsevier.com/locate/rser

A comprehensive analysis of time-dependent performance of a solar chimney power plant equipped with a thermal energy storage system

Amir Arefian [a], Reza Hosseini-Abardeh [a], Mohsen Rahimi-Larki [b], Arman Torkfar [a], Hamid Sarlak [c,*]

[a] Mechanical Engineering Department, Amirkabir University of Technology (Tehran Polytechnic), Tehran, Iran
[b] Department of Mineral Resource Engineering, Chair of Ceramics, Montanuniversitäte Leoben, Austria
[c] Department of Wind and Energy Systems, Technical University of Denmark, Denmark

ARTICLE INFO

Keywords:
Solar chimney power plant
Thermal energy storage
Thermal effusivity
Heat penetration depth
Capacity factor
Power generation quality factor

ABSTRACT

Solar Chimney Power Plants (SCPP) are among the promising solar thermal electricity generation technologies. Equipped with a Thermal Energy Storage (TES) system, such technologies can overcome variations in the main driving factors such as solar radiation and ambient air temperature. This article presents a comprehensive semi-analytical model of a TES to predict the time-dependent performance of an SCPP. By introducing a Quality Factor of power generation (QF) that includes energy conversion efficiency and capacity factor, the effects of 15 TES materials have been studied on the plant performance. Results indicate no significant difference between water TES and clay or soil type, and water-filled bags or tubes are relatively ineffective in improving performance compared to them. Among the various TES materials analyzed, a type of wet soil, i.e., the specific wet mixture of clay, sand, and silt in closed and dark-colored bags, show excellent performance in both QF enhancement and having low Heat Penetration Depth (HPD) simultaneously. The QF and HPD are directly affected by thermal effusivity and thermal diffusivity, respectively. Implementing wet soil TES for the studied power plant (Manzanares) enhances the QF from 7.46 % (for limestone soil) to 10.95 %. Water-filled bags demonstrate a heat penetration depth of 0.4 m, while wet soil exhibits a slightly greater depth of 0.5 m. Furthermore, water-filled bags experience a broader temperature range of 40 °C, whereas wet soil undergoes a comparatively smaller temperature variation of 26 °C. Furthermore, the capacity factor raises from 41.18 % to 61.07 % when utilizing wet soil TES compared to water-filled bags.

1. Introduction

Power generation strategies are expected to undergo major changes in the near future due to economic, political, and environmental factors. The use of renewable energy, especially solar power, is likely to increase significantly. However, since solar and wind energy sources are intermittent, they cannot meet the variable demand for electricity throughout the year. Energy storage is proposed to provide a stable and reliable energy supply, reducing fluctuations in output power for renewable technologies [1,2].

The focus of this study is to investigate the performance of Solar Chimney Power Plants (SCPP), a relatively new solar thermal technology, under varying environmental conditions and in connection with Thermal Energy Storage (TES) systems. SCPPs work by heating air under a transparent cover using solar radiation and the greenhouse effect, causing the air to rise due to buoyancy. A part of the thermal energy is converted into kinetic energy in the chimney and leads to electric power generation in the aero turbine and generator set. Unlike other solar concentrating technologies, SCPPs can absorb both beam and diffuse solar radiation [3]. A diagram of the process is shown in Fig. 1. The Solar Chimney Power Plant (SCPP) can operate even on cloudy days using thermal energy storage. The ground beneath the solar collector absorbs solar radiation during the day and transfers it to the air during periods without radiation, such as at night. If equipped with a thermal storage system, an SCPP can generate electricity consistently throughout the year. Notably, without proper TES, the output power of the SCPP can vary significantly during different times of day and throughout the year.

* Corresponding author. Aero and Fluid Dynamics Section, Department of Wind and Energy Systems, Technical University of Denmark, 2800 Kongens Lyngby, Denmark.

E-mail addresses: a.arefian@aut.ac.ir (A. Arefian), hoseinir@aut.ac.ir (R. Hosseini-Abardeh), mohsen.rahimilarki@unileoben.ac.at (M. Rahimi-Larki), arman.torkfar@aut.ac.ir (A. Torkfar), hsar@dtu.dk (H. Sarlak).

https://doi.org/10.1016/j.rser.2023.114051
Received 23 June 2023; Received in revised form 30 October 2023; Accepted 31 October 2023

Nomenclature

A	Surface area [m^2]
b	Thermal effusivity [Ws$^{0.5}$/m^{2}K]
CF	Capacity factor
c	Specific heat capacity [J/kgK]
D	Diameter [m]
E	Generate Electrical Energy [J]
f	Friction factor
G	Solar radiation intensity [W/m^2]
g	Gravitational acceleration [m/s^2]
H	Height, depth [m]
HPD	Heat Penetration Depth [m]
h	Heat transfer coefficient [W/m^{2}K], Enthalpy [J/kg]
k	Thermal conductivity [W/mK], Pressure drop coefficient
$\dot{m}$	Mass flow rate [kg/s]
P	Power [kW]
p	Pressure [Pa]
Q	Thermal energy [J]
QF	Quality factor of power generation
$\dot{q}''$	Heat flux [W/m^2]
R	Radius [m]
Re	Reynolds number
r	Radial coordinate [m]
T	Temperature [°C]
t	Time [s]
u	Radial velocity [m/s]
$\dot{V}$	Volumetric flow rate [m^3/s]
v	Axial velocity [m/s], Specific volume [m^3/kg]
$\dot{W}$	Fluid power [W]
z	Axial coordinate [m]

Greek Symbols

α	Absorptivity, Thermal Diffusivity [m^2/s]
χ	Turbine pressure drop ratio
Δ	Difference
ε	Emissivity, surface roughness [m]
γ	Heat capacity ratio
η	Efficiency
κ	Polytropic index
μ	Dynamic viscosity [kg/ms]
ρ	Density [kg/m^3]
σ	Stefan-Boltzmann constant [W/m^{2}K^4]
τ	Transmissivity, Time [s]

Indexes and subscripts

II	Second law of thermodynamics
∞	Ambient
$\infty,0$	Ambient condition at ground level
∞,H_{chim}	Ambient condition at chimney height
ACW	Ambient crosswind
$avail.$	Available
ca	Collector inside air
ci	Collector inlet
cg	Collector ground
$cgcr$	Collector ground to roof
$chim$	Chimney
$chim,f$	Chimney frictional
$chim,i$	Chimney inlet
$chim,o$	Chimney outlet
co	Collector outlet
$coll$	Collector
$coll,f$	Collector frictional
cr	Collector roof
$crca$	Collector roof to inside air
$crcg$	Collector roof to ground
$crsky$	Collector roof to sky
dyn	Dynamic
$elec.$	Electrical
$HTVT$	Horizontal to vertical transition
h	Horizontal, hydraulic
hyd	Hydrostatic
max	Maximum
n	Spatial node
PCU	Power Conversion Unit
$stor$	Storage
sw	Short wavelength
TES	Thermal Energy Storage
TES,i	Initial conditions for TES
tg	Turbo-generator set
th	Thermal
TL	Total loss
tot	Total driving
$turb$	Turbine
$turb,i$	Turbine inlet
$turb,o$	Turbine outlet
$WIPD$	Wind-induced pressure drop
z	Axial coordinate

The first operational pilot of a solar chimney power plant was built in Manzanares, Spain, in the early 1980s. The dimensions of the plant included a chimney height of 195 m and a radius of 5.08 m, along with a collector radius of 122 m and a height of 1.85 m [4–7]. A temperature rise in the collector of up to 17 °C and an average updraft velocity reached 12 m/s were achieved, gaining a rated power of 50 kW and a maximum actual output power of 41 kW [8].

The Manzanares prototype has yielded significant results, leading to numerous research studies and accelerating the development of solar chimney technology. Due to fluctuations in solar energy input and ambient temperature, thermal energy storage has become a critical area of interest in SCPP technology. Ming [9] conducted one of the CFD investigations into thermal energy storage in a solar chimney power plant. By treating the thermal storage layer as a porous material, he concluded that materials with higher thermal conductivity, such as sand, are better suited for the thermal storage unit due to their enhanced ability to absorb heat during daylight hours. Fanlong et al. [10] showed that the ratio between the maximum and minimum power generation in a 100 MW SCPP equipped with natural soil thermal storage would be more than 20 during the day and night. They showed that this could be significantly reduced by using artificial thermal storage water-filled transparent bags with volumetric absorption. The output power has become saturated and stable for a water layer thickness of 0.1 m. Chaichan and Kazem [11] carried out an experimental investigation of the effect of concrete, black concrete, and black gravel beds as TES in the climate of Baghdad. The results showed that black gravel had performed better than the other two mediums. They suggested that any enhancement in collector bed radiation properties, such as coating with a special black color, can significantly improve the performance. Ming et al. [12] conducted research on the problem of output power fluctuations in solar chimney power plants (SCPP) and presented an innovative approach involving a hybrid energy storage system utilizing water and sandstone. The researchers developed mathematical models to assess the influence of the energy storage layer on output power. Furthermore, they investigated the effects of collector surface occupancy and the placement of the thermal energy storage (TES) system. The findings indicate that the hybrid system successfully mitigates power fluctuations, resulting in improved power generation stability. Moreover, the study identifies an optimal thickness for the TES layer, maximizing its effectiveness in power smoothing. Hurtado et al. [13] conducted a simulation study to investigate the effect of soil thermal inertia on the performance of SCPP by analyzing the experimental results of the Manzanares prototype. Using a transient numerical model, they demonstrated that compacted soil could improve the output power by 10 % compared to the reference case. Bernardes and Zhou [14] conducted an analytical-numerical study on heat storage and release in thermal storage, intending to present the effect of water-filled bags on conductive and convective heat flows and absorption of solar radiation. The main parameter was the water layer thickness, which was investigated with and without considering the effect of thermal insulation due to thermal stratification in the storage depth. A similar study conducted by Bernardes [15] focuses on analyzing the sensible heat storage process in a Solar Updraft Tower collector. The research investigates the transient heat transfer in typical soils, considering conduction, convection, and solar radiation. The simulations reveal complex thermal behavior in different soil materials, indicating that those with lower thermal effusivity and diffusivity can effectively reduce output peaks during periods of high heat gains. Larbi et al. [16] developed mathematical modeling of an SCPP performance. Based on the results, equipping the plant with artificial thermal storage has only reduced the extreme changes in the output power during the day hours and has not had much effect on the nighttime performance. Li et al. [17] investigated the effect of geometrical parameters on plant performance, including chimney height, collector diameter, and TES layer thickness. TES was modeled one-dimensionally based on the available analytical solutions. They also defined a power quality index for an SCPP, which includes both the concepts of efficiency and stability. Results indicated that the power quality factor directly depends on chimney height while inversely related to the collector diameter. Choi et al. [18] conducted a study on a large-scale solar chimney power plant (SCPP) and examined its performance with and without a water storage system. They developed an analytical lumped body model to analyze the system. The findings of their study revealed that the inclusion of a water storage system substantially increased the power output of the SCPP. They also conducted a parametric study and found that the output power reached its maximum value when the turbine pressure drop ratio was set at 0.75, deviating from the previously assumed value of 2/3. Bashirnejad et al. [19] investigated the effect of a phase change material (PCM) as a thermal energy storage on a laboratory-scale SCPP. By examining the effect of three materials, soil, water, and paraffin, the results indicated an increase of 9 and 20 % for the duration of power generation and 6.2 and 22 % in the amount of electrical energy production for water and paraffin compared to the system without an artificial TES. Notably, the presence of the aero turbine was not considered, and its mutual effect on the plant performance was not observed. Yaswanthkumar and Chandramohan [20,21] conducted steady-state numerical modeling of the flow parameters in an SCPP with and without thermal storage. Results showed that thermal storage causes the pressure, temperature, and velocity to decrease because of the accumulation of part of the energy in thermal storage. Sediqi et al. [22] performed a numerical study of an SCPP by applying different values for turbine pressure drop and soil porosity. The plant efficiency and power generation capacity have been increased by reducing the porosity of the soil in the collector. The effects of time delay and energy storage by the TES layer have not been captured. Maia and Silva [23] performed a thermodynamic assessment of a 2.5 m chimney height small-scale SCPP using a comprehensive unsteady model for airflow. TES surface temperature was estimated

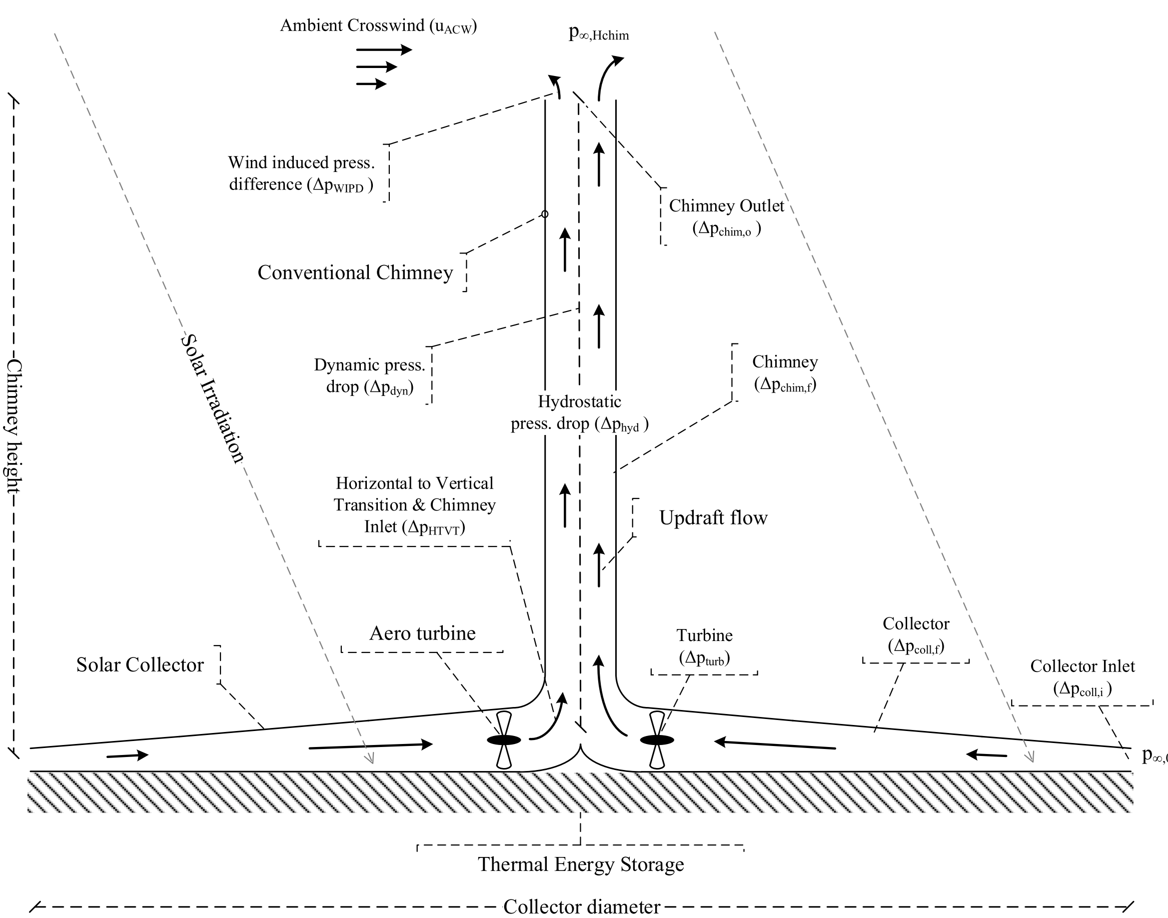

Fig. 1. A schematic of a conventional SCPP and pressure drop terms for momentum analysis.

using a closed-form solution for one-dimensional transient heat conduction. Based on the results for the no-load condition, about 60 % of incident solar energy was absorbed in the TES, 28 % was wasted as thermal losses, and only 12 % was used for airflow heating. Exergy analysis showed that only 13 % of input exergy had been used by airflow. Ikhlef et al. [24] conducted an experimental study on the effect of various TES systems on the performance of a small-scale SCPP in Isparta, Turkey. The chimney height and collector diameter were 4.2 m and 5.93 m, respectively. Findings revealed that the collector efficiency strongly depended on thermal storage, and crushed gravel basement was the best TES with a collector efficiency of 89.73 % compared to asphalt, sand, sand + water-filled tubes. Cuce et al. [25] concluded that there is no significant difference between the performance of an SCPP equipped with natural sand or gravel a the TES material. Their steady-state numerical simulation showed that both materials give the Manzanares model output power of 41.636 kW at a radiation intensity of 800 W/m^2. Méndez and Bicer [26] performed a similar numerical study for steady-state and time-dependent scenarios. Results showed that the bismuth-led-tin-cadmium and magnesium chloride hexahydrate provide the highest power generation between PCMs with an annual-averaged output power of 27.46 kW and a storage temperature of about 73 °C. Sensible thermal storage formed by sandstone gave the highest output power of 31.49 kW and an average storage temperature of 80 °C. The highest annual-averaged energy and exergy efficiencies of 0.122 % and 0.128 % were achieved using the sandstone TES. Guo et al. [27] examined loamy sand and two hypothetical soils, including light dry soil and wet sand as TES medium by developing a numerical model. Comparison between steady and unsteady performance showed that electricity generation is 31.26 % higher in unsteady simulation by assuming a 4 m depth for the storage layer.

As revealed by the literature review, previous studies have predominantly focused on the heat capacity of thermal storage in SCPP and have typically modeled this system as a uniform-temperature or lumped body. While certain studies have addressed heat penetration and temperature distribution within the thickness of the heat storage layer, less attention has been given to understanding the impact of this system on crucial performance parameters of the solar chimney power plant, such as the updraft velocity inside the chimney, the outlet temperature of the collector, and ultimately the output power. Therefore, conducting a comprehensive and well-validated study, supported by experimental data, becomes essential to examine the complete range of effects that the presence and alteration of thermal storage may have on the dynamic and time-dependent performance of SCPP. This research aims to fill this gap by developing a comprehensive semi-analytical model to investigate the time-dependent behavior of an SCPP with thermal storage under three driving factors: solar radiation, ambient temperature, and ambient crosswind. The simulation results have been validated with experimental data from the Manzanares power plant, and various performance parameters have been evaluated using performance indicators. The study also analyzes the heat penetration depth during daily operation and proposes optimal thermal storage. One of the primary objectives of this research is to assess the potential for mitigating power generation fluctuations in solar chimney power plants. To achieve this goal, the study employs a comprehensive and integrated modeling approach encompassing various power plant subsystems. An essential aspect of the research involves accurately estimating the dynamic behavior of heat storage using different materials. By accomplishing these objectives, the study aims to provide valuable insights into effectively reducing power generation fluctuations in solar chimney power plants.

2. Mathematical model

This section has developed the governing equations of flow and heat transfer, including energy, momentum, and mass conservation laws for a conventional SCPP. Model development is mainly based on zero-dimensional analysis and the control volume approach except where specified. For example, the temperature distribution in a thin layer of the collector cover, i.e., glass or plastic, is logically negligible. This issue will not be physical for the thick layer of natural or artificial thermal storage, whose function is to store and release thermal energy due to temperature changes in its different layers. The basic assumptions made in this modeling are:

1 The working fluid is dry air, considered an ideal gas with constant specific heat capacity (cold air approximation).
2 Thermal inertia is considered only for the TES layer. Other components, such as collector cover or solar chimney, have a low thickness and are modeled in a quasi-steady condition. Also, due to the low frequency of the main affecting factors, the temporal changes of fluid mass inertia are ignored, and the momentum equation is analyzed in a steady-state manner.
3 The effect of ambient wind entering the solar collector and mixing with the heating air has been ignored.
4 The chimney is insulated, and the updraft flow experiences an adiabatic process.
5 The effects of pressure drop caused by the radial reinforcement structures along the chimney and the structural network supporting the collector roof are not considered.
6 Fluid flow and heat transfer in the solar chimney system have axial symmetry.
7 The aero turbine has been considered adiabatic and reversible (isentropic).

2.1. Energy conservation

Considering the priority of thermal energy in creating a natural draft in an SCPP, the governing equations of energy are developed and explained first. The equivalent thermal network for a solar collector is shown in Fig. 2. Due to the small thickness of the roof cover, its conductive heat transfer is ignored, and it is modeled as a lumped body without thermal inertia. The energy conservation equation for the collector roof is presented in equation (1).

$$G_{cr} = h_{\infty}(T_{cr} - T_{\infty}) + h_{crsky}\left(T_{cr} - T_{sky}\right) + h_{crca}(T_{cr} - T_{ca}) + h_{crcg}\left(T_{cr} - T_{cg}\right) \tag{1}$$

A part of the solar radiation, proportional to the short-wavelength absorption coefficient, is absorbed in the layer. It is used for convection heat loss from the roof to the ambient air, radiation heat loss from the roof to the sky, convective heat exchange with the air passing through the collector, and long-wavelength radiative heat transfer with the ground surface. Equation (2) models a part of the global solar insolation (GHI) absorbed in the collector cover [28].

$$G_{cr} = \alpha_{cr(SW)} G_h \tag{2}$$

The convection heat transfer coefficient h_{∞} caused by the combined effect of the natural convection from a horizontal flat plane and ambient crosswind flow over the collector roof is estimated based on the Jurges empirical relation [29]:

$$h_{\infty} = 5.7 + 3.8 u_{wind} \tag{3}$$

The heat transfer coefficient h_{crsky} , which is related to long-wave radiation from the collector cover to the sky, is calculated by equation (4) applied to a flat plane [28].

$$h_{crsky} = \sigma\, \varepsilon_{cr}\left(T_{cr}^2 + T_{sky}^2\right)\left(T_{cr} + T_{sky}\right) \tag{4}$$

Sky temperature in Kelvin can be calculated by equation (5) [30].

$$T_{sky} = 0.0552 T_{\infty}^{1.5} \tag{5}$$

The internal convection heat transfer coefficient of the solar collector

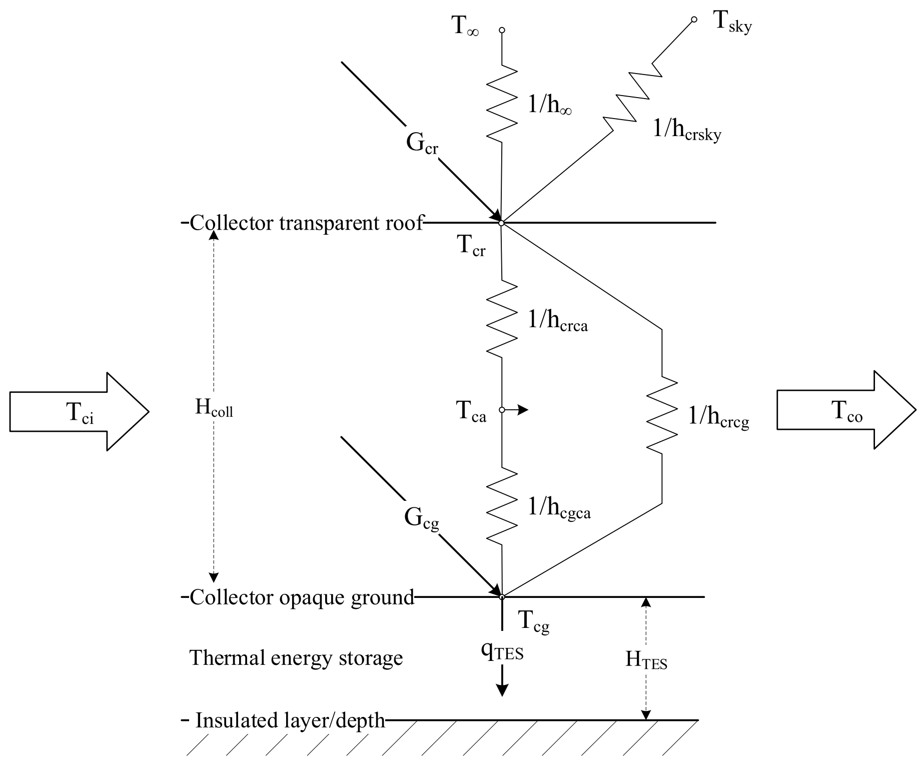

Fig. 2. Thermal network associated with a solar collector.

can be evaluated by the empirical equation of Gnielinski [29,31,32]. Equation (6) can be implemented for all conditions that the temperature of the collector roof and inside flowing air may take in daily operation.

$$h_{crca} = \frac{(f_{coll}/8)(\mathrm{Re}-1000)\mathrm{Pr}}{1+12.7(f_{coll}/8)^{1/2}(\mathrm{Pr}^{2/3}-1)}\left(\frac{k}{D_{h,coll}}\right) \tag{6}$$

It is valid with an error of ±10 % compared to experimental results for the Reynolds number 2300 to 5,000,000 and the Prandtl number 0.5 to 2000 [33]. For transient and fully developed turbulent flow, and assuming the flow between two rough and parallel plates in the solar collector, the Haaland equation [34,35] is used for the friction coefficient according to equation (7).

$$f_{coll} = \begin{cases} 0.3086\left[log_{10}\left(\left(\frac{6.9}{\mathrm{Re}}\right)+\left(\frac{\varepsilon/D_{h,coll}}{3.75}\right)^{1.11}\right)\right]^{-2} & \varepsilon/D_{h,coll} > 10^{-4} \\ 2.7778\left[log_{10}\left(\left(\frac{7.7}{\mathrm{Re}}\right)^{3}+\left(\frac{\varepsilon/D_{h,coll}}{3.75}\right)^{3.33}\right)\right]^{-2} & \varepsilon/D_{h,coll} \le 10^{-4} \end{cases} \tag{7}$$

In a conventional configuration of an SCPP, the solar collector has been considered as two parallel disks with a converging flow. By applying the general definition [36], the hydraulic diameter can be obtained according to equation (8). The Reynolds number is also obtained using equation (9), and the average velocity inside the collector is evaluated by equation (10) [37].

$$D_{h,coll} = \frac{4A}{P} = \frac{4(2\pi r H_{coll})}{2(2\pi r)} = 2H_{coll} \tag{8}$$

$$\mathrm{Re} = \frac{\overline{\rho}_{coll}\overline{u}_{coll}D_{h,coll}}{\mu} \tag{9}$$

$$\begin{aligned}\overline{u}_{coll} &= \frac{1}{R_{coll}-R_{chim}}\int_{r=R_{chim}}^{r=R_{coll}} u_{coll}\,dr = \frac{1}{R_{coll}-R_{chim}}\int_{r=R_{chim}}^{r=R_{coll}} \frac{\dot{m}}{2\rho\pi r H_{coll}}dr \\ &= \frac{\dot{m}}{2\overline{\rho}_{coll}\pi H_{coll}(R_{coll}-R_{chim})}\ln\left(\frac{R_{coll}}{R_{chim}}\right)\end{aligned} \tag{10}$$

Long-wave radiation heat transfer in the solar collector is like two parallel flat plates. The equivalent radiation heat transfer coefficient inside the collector is calculated by equation (11) using the long-wavelength emissivity coefficients [28].

$$h_{crcg} = \sigma\frac{\left(T_{cr}^2+T_{cg}^2\right)\left(T_{cr}+T_{cg}\right)}{\frac{1}{\varepsilon_{cr}}+\frac{1}{\varepsilon_{cg}}-1} \tag{11}$$

The energy conservation equation for the surface layer of the collecting bed is expressed according to equation (12).

$$G_{cg} = h_{cgcr}\left(T_{cg}-T_{cr}\right)+h_{cgca}\left(T_{cg}-T_{ca}\right)+\dot{q}^{''}_{TES} \tag{12}$$

where

$$G_{cg} = \tau_{cr(SW)}\alpha_{cg(SW)}G_h \tag{13}$$

The equivalent radiation heat transfer coefficient of the ground surface to the collector roof equals the heat transfer coefficient of the cover to the ground surface, i.e.:

$$h_{cgcr} = h_{crcg} \tag{14}$$

Also, the Gnielinski relation expressed in equation (6) is valid in all conditions related to the hot or cold plate facing downwards or upwards. Thus, the same relation is used to calculate the convection heat transfer coefficient for the ground surface, i.e.:

$$h_{cgca} = h_{crca} \tag{15}$$

The last term of the right-hand side of equation (12) is related to conduction heat transfer and heat penetration into the collector bed, which can be natural or artificial TES. Thermal storage modeling is performed transiently with a distributed or non-isothermal body. Since the conductive heat transfer in the radial direction is much lower than in the axial direction, the thermal energy storage layer can be accurately modeled in one dimension [14,20,21,29]. In this condition, conduction heat transfer occurs in the depth of the storage layer, reaching a bottom insulated boundary, which has been considered for both natural and artificial TESs [17,38]. The governing equation for one-dimensional transient heat conduction in a TES medium is the 1-D Fourier-Biot diffusion equation presented in equation (16) [39,40].

$$\frac{\partial T_{TES}(\tau,z)}{\partial \tau}=\frac{k_{TES}}{c_{TES}\rho_{TES}}\frac{\partial^2 T_{TES}(\tau,z)}{\partial z^2} \tag{16}$$

The initial condition for solving equation (16) is the equality of all temperature values in the depth of the TES with a constant value, which is usually considered the ambient temperature, i.e.:

$$T_{TES}(0,z)=T_{TES,i}=T_{\infty,i} \qquad 0<z<H_{TES} \tag{17}$$

Equation (16) has two Neumann boundary conditions for analyzing the thermal storage of an SCPP [39]. At the surface of the collecting bed, the heat flux exchanged with its other components, i.e., $\dot{q}''_{TES}$, is equal to the amount of thermal conduction at the boundary. Equation (18) is established as the first boundary condition.

$$\frac{\partial T_{TES}(\tau,0)}{\partial z}=-\frac{\dot{q}''_{TES}}{k_{TES}} \qquad \tau>0 \tag{18}$$

$$\dot{W}_{avail.}=\dot{m}\Delta h_{turb}=\dot{m}\int v\,dp\simeq\frac{\dot{m}}{\overline{\rho}_{turb}}\Delta p_{turb}=\dot{V}_{turb}\Delta p_{turb} \tag{21}$$

$$\dot{W}_{elec}=\eta_{tg}\dot{W}_{avail} \tag{22}$$

The outlet temperature of the aero turbine, which is equal to the inlet temperature of the chimney, is calculated according to equation (23) using isentropic relations for air.

$$T_{turb,o}=T_{turb,i}\left(\frac{p_{turb,o}}{p_{turb,i}}\right)^{\frac{\gamma-1}{\gamma}}=T_{turb,i}\left(\frac{p_{turb,i}-\Delta p_{turb}}{p_{turb,i}}\right)^{\frac{\gamma-1}{\gamma}} \tag{23}$$

Updraft air experiences an adiabatic ascent process by assuming an insulated chimney wall. Equation (24) is valid for the control volume of the chimney due to the negligible viscous heating [42].

$$\dot{m}\,c_p\left(T_{chim,i}-T_{chim,o}\right)=\dot{m}\,g\,H_{chim} \tag{24}$$

2.2. Momentum conservation

The momentum conservation equation governs the pressure drop or changes in a solar chimney cycle, as shown in Fig. 1. Starting from a point near the collector inlet where the pressure is equal to the ambient air, $p_{\infty,0}$ to a point near the chimney outlet where ambient air reaches the pressure $p_{\infty,H_{chim}}$, equation (25) reads:

$$p_{\infty,0}-\Delta p_{coll,i}-\Delta p_{coll,f}-\Delta p_{turb}-\Delta p_{HTVT}-\Delta p_{hyd}-\Delta p_{chim,f}-\Delta p_{chim,o}-\Delta p_{dyn}-\Delta p_{WIPD}=p_{\infty,H_{chim}} \tag{25}$$

Also, applying the insulation condition or the constant temperature at the insulated boundary gives the second boundary condition according to equation (19) [20].

$$\frac{\partial T_{TES}(\tau,H_{TES})}{\partial z}=0 \qquad \tau>0 \tag{19}$$

It should be noted that in the presented modeling, by applying two Neumann conditions at the boundaries for the thermal storage, no prejudicial and binding conditions regarding the storage temperature and, specifically, its depth temperature have not been imposed on the problem. On this basis, the thermal storage will reach its permanent behavior under the primary and intermittent driving forces, i.e., solar radiation and ambient temperature. This issue is vital compared with other research, such as the modeling by Li et al. [17].

The governing equation for the energy of flowing air inside the collector is expressed according to equation (20).

$$h_{crca}(T_{cr}-T_{ca})+h_{cgca}\left(T_{cg}-T_{ca}\right)=\frac{\dot{m}\,c_{p,a}}{A_{coll}}(T_{co}-T_{ci}) \tag{20}$$

Assuming an isentropic turbine, the power that can be extracted from the fluid flow is calculated using the Gibbs equation [41] taken in equation (21). The electrical output power from the plant is estimated by equation (22) using turbo-generator efficiency η_{tg}.

The above equation can be rewritten as the sum of the hydrostatic pressure difference outside the chimney and the hydrostatic pressure drop inside, the turbine pressure drop, and total pressure loss. The left side of equation (26) is the driving force in an SCPP, and the right-hand side is the resistance force.

$$p_{\infty,0}-p_{\infty,H_{chim}}-\Delta p_{hyd}=\Delta p_{turb}+\Delta p_{TL} \tag{26}$$

Considering the entire expression on the left side of equation (26) as the total pressure difference, the integral relation (27) is obtained [43–45].

$$\Delta p_{tot}=p_{\infty,0}-p_{\infty,H_{chim}}-\Delta p_{hyd}=\int_{z=0}^{z=H_{chim}}\rho_\infty(z)\,g\,dz-\int_{z=0}^{z=H_{chim}}\rho_{chim}(z)\,g\,dz=\int_{z=0}^{z=H_{chim}}(\rho_\infty(z)-\rho_{chim}(z))\,g\,dz \tag{27}$$

For updraft air which experiences an adiabatic process inside the chimney, using equation (24) and ideal gas relations, the density distribution along the chimney can be determined as equation (28) [35,46].

$$\rho_{chim}(z)=\rho_{chim,i}\left(1-\frac{\gamma-1}{\gamma}\frac{z}{H_0}\right)^{1/(\gamma-1)} \tag{28}$$

where $H_0=R_lT_{chim,0}/g$ and $\gamma=1.4005$ is the specific heat ratio. For a non-adiabatic process for air outside the chimney, the temperature lapse rate equals 0.0065 K/m (standard atmosphere), which can be used from the ground surface to a height of 11 km [31,41,47]. In this case, equation (28) can be used for air outside the chimney by replacing γ by $\kappa=1.235$.

The power conversion unit imposes the turbine pressure drop on the system; however, its operating value is always between zero and the total driving pressure difference. The parameter χ defined as the ratio of turbine pressure drop to the total pressure difference is used to model turbine pressure drop according to equation (29) [48–50].

$$\Delta p_{turb} = \chi \Delta p_{tot} \qquad 0 \le \chi \le 1 \tag{29}$$

The term Δp_{TL} includes all pressure loss factors in the solar chimney cycle. Except Δp_{WIPD}, all other factors are only a function of the velocity created in the system; in other words, they are a coefficient of dynamic pressure. Pressure drop terms mentioned in relation (25) are discussed in the following. The local pressure drop at the collector inlet is modeled according to equation (30).

$$\Delta p_{coll,i} = k_{coll,i}\ \frac{1}{2}\rho_{coll,i} u_{coll,i}^2 = k_{coll,i}\ \frac{1}{2}\frac{\dot{m}^2}{\rho_{coll,i} A_{coll,i}^2} \tag{30}$$

where $k_{coll,i}$ is the pressure drop coefficient considered for a sudden contraction equals unity [36]. Using the hydraulic diameter of the solar collector and Darcy friction factor [44], modeling the frictional pressure drop in the collector is done according to equation (31).

$$\Delta p_{coll,f} = f_{coll} \frac{R_{coll} - R_{chim}}{D_{h,coll}}\ \frac{1}{2}\overline{\rho}_{coll} \overline{u}_{coll}^2 \tag{31}$$

The pressure drop for the chimney inlet and the area related to the change in the flow direction, i.e., horizontal to vertical transition (HTVT) region, is modeled using equation (32) [51].

$$\Delta p_{HTVT} = k_{HTVT}\ \frac{1}{2}\rho_{chim,i} u_{chim,i}^2 \tag{32}$$

The pressure drop coefficient k_{HTVT} for the bellmouth configuration of the chimney inlet is calculated based on equation (33) [51]. For a typical ratio of 0.12, the inlet pressure drop coefficient equals 0.09 [52].

$$k_{HTVT} = 0.5\exp\left(-14.114\frac{r}{D_h}\right) \tag{33}$$

The frictional pressure drop inside the chimney is calculated by equation (34), where f_{chim} is a rounded pipe friction coefficient [44].

$$\Delta p_{chim,f} = f_{chim}\frac{H_{chim}}{D_{chim}}\ \frac{1}{2}\overline{\rho}_{chim} v_{chim}^2 = f_{chim}\frac{H_{chim}}{D_{chim}}\ \frac{1}{2}\frac{\dot{m}^2}{\overline{\rho}_{chim} A_{chim}^2} \tag{34}$$

The flow geometry at the chimney outlet is considered a sudden expansion whose coefficient $k_{chim,o}$ equals 0.058 [45]. The pressure drop in this area is modeled using equation (35).

$$\Delta p_{chim,o} = k_{chim,o}\ \frac{1}{2}\rho_{chim,o} v_{chim,o}^2 = k_{chim,o}\frac{1}{2}\frac{\dot{m}^2}{\rho_{chim,o} A_{chim}^2} \tag{35}$$

Even without irreversible factors in the system, i.e., minor and major pressure drop terms, the total driving pressure difference leads to the flow acceleration from the collector inlet to the chimney outlet and creates a dynamic pressure drop according to equation (36) [41].

$$\Delta p_{dyn} = \frac{1}{2}\overline{\rho}_{chim} v_{chim}^2 = \frac{1}{2}\frac{\dot{m}^2}{\overline{\rho}_{chim} A_{chim}^2} \tag{36}$$

Investigating the complex effect of the ambient crosswind (ACW) on the updraft flow in the solar chimney is not the purpose of this work and can be found in the previous studies conducted by authors [53–55]. It is often assumed that the power plant is built in a geographical location with a negligible prevailing wind speed. However, the pressure drop caused by ACW at the chimney outlet is estimated by equation (37).

$$\Delta p_{WIPD} = k_{ACW}\frac{1}{2}\rho_{\infty,H_{chim}} u_{ACW}^2 \tag{37}$$

The pressure drop coefficient k_{ACW} is calculated according to the experimental relationship of Du Preez [34,56]. It is valid for the interval $1.8 \le u_{ACW}/v_{chim,o} \le 24$ and has an acceptable estimate for outside values. This study assumes the ratio of throttling and geometrical cross-sections as unity, and the simplified equation (38) has been used [56].

$$k_{ACW} = -0.405 + 1.07\left(\frac{u_{ACW}}{v_{chim,o}}\right) + 1.8\log_{10}\left[\left(\frac{u_{ACW}}{2.7 v_{chim,o}}\right)\right] \times \left(\frac{u_{ACW}}{v_{chim,o}}\right)^{-2} \tag{38}$$

2.3. Mass conservation

As mentioned, an SCPP has a single-flow geometry in its conventional configuration. Based on mass conservation, equation (39) is valid and can be used anytime.

$$\dot{m}_{coll} = \dot{m}_{PCU} = \dot{m}_{chim} \tag{39}$$

The mass flow rates are defined based on the flow parameters and fluid local properties according to equations (40) and (41).

$$\dot{m}_{coll} = \rho_r u_r A_r = 2\pi r \rho_r u_r H_{coll} \tag{40}$$

$$\dot{m}_{chim} = \rho_z v_z A_{chim} = \pi R_{chim}^2 \rho_z v_z \tag{41}$$

3. Mathematical representation and numerical method

The governing equations of a TES and the other governing equations of the system, which are of algebraic type, have formed a set of 250 non-linear and coupled Differential-Algebraic Equations (DAE). The intended DAE system has M algebraic variables such as updraft velocity, collector surface temperature, chimney inlet temperature, and $N-1$ differential variables related to the discretized points of different layers of a TES. In order to convert the differential part of the equations from partial to ordinary derivatives, the discretization of the Fourier-Biot equation (16) is done only in space, and its transient term remains unchanged for integration by the solver. Partial derivatives become discretized using the second-order central in-space discretization scheme [57], as shown in equation (42).

$$\left[\frac{dT_{TES}}{d\tau}\right]_n = \left[\frac{\lambda_{TES}}{c_{TES}\rho_{TES}}\right]_n \left(\frac{[T_{TES}]_{n+1} - 2[T_{TES}]_n + [T_{TES}]_{n-1}}{\Delta z^2}\right) \qquad 1 \le n \le N-1 \tag{42}$$

where n is the index of axial nodes through a TES and $\Delta z = H_{TES}/N$. The boundary condition (18) related to the upper surface of thermal storage is discretized based on a second-order forward in-space scheme according to equation (43) [57].

$$\frac{-3[T_{TES}]_0 + 4[T_{TES}]_1 - [T_{TES}]_2}{2\Delta z} = \left[-\frac{\dot{q}''_{TES}}{\lambda_{TES}}\right]_0 \tag{43}$$

Finally, the boundary condition (19) related to the insulated or constant-temperature depth of thermal storage is discretized with a second-order backward in-space scheme [57] according to equation (44).

$$\frac{3[T_{TES}]_N - 4[T_{TES}]_{N-1} + [T_{TES}]_{N-2}}{2\Delta z} = 0 \tag{44}$$

Engineering Equation Solver (EES) software has been used for programming, solving, post-processing, and extracting the results of the developed mathematical model [58,59].

4. Results and discussion

The Manzanares power plant configuration is used as the case study in this research. First, the dimensional specifications, properties of the materials used, and the design and operation conditions of this power plant have been reviewed. Then, the results of the reference case simulation were verified with the experimental data of the Manzanares prototype.

In the following, the effect of the change in the heat storage medium on the time-dependent performance of an SCPP has been studied by examining 14 TES materials in addition to the reference ones. Also, the average and integral properties of performance parameters have been

Table 1
Technical specifications and design criteria of Manzanares power plant [7].

Parameter	Value
Tower Height, H_T	194.6 m
Tower radius, R_T	5.08 m
Mean collector radius, R_c	122 m
Average canopy height	1.85 m
No. of turbine blades	4
Blade radius	5.0 m
Operating modes	a) stand-alone operation with variable speed (optimum utilization of upwind energy) b) grid connection mode
Turbine speed in grid connection mode	100 rpm
Gear ratio	1:10
Design irradiation	1000 W/m^2
Design fresh-air temperature	302 K
Temperature increase, mean for model assumption at design point	20 K
Collector efficiency, mean for model assumption at design point	0.32
Turbine efficiency	83 %
Friction loss factor	0.90
Upwind velocity under load conditions	9 m/s
Upwind velocity on release	15 m/s
Power output, mean for model assumptions at design point	50 kW

investigated in the form of indices. Finally, the issue of thermal penetration depth in a TES has been discussed.

4.1. Manzanares prototype design and performance data

The experimental data of the Manzanares power plant, as the first medium-scale SCPP with research application, is the most cited experimental data in this technology field, which has been used in a wide range of studies [29,51,60–63]. Design data, environmental conditions, and performance results have been collected and published by Haaf et al. [5,7]. Technical information and design criteria of the Manzanares power plant have been brought in Table 1. The optical properties of the solar collector ground surface were improved using a layer of natural bitumen, and its absorption coefficient was increased to 0.91 [5].

4.2. Validation of simulation results

Discrete experimental data of driving factors, i.e., global horizontal insolation and ambient temperature for the second day of September 1982, are shown in Fig. 3. Interpolated curves were generated based on experimental data and applied to the mathematical model as inputs. The ground medium was limestone soil with a density of 1900 kg/m^3, a specific heat capacity of 840 J/kg-K, and an average thermal conductivity of 0.75 W/m-K [5]. An adiabatic thermal stratification has been reported for the air inside and outside the system. The collector transparent roof was made of PVF and PVC materials with a thickness of 0.1 mm [7].

The temperature difference created in the solar collector is the main indicator of collector thermal performance and directly affects the total pressure difference. Fig. 4 compares experimental and simulated values of the Manzanares power plant. Notably, in all similar figures, the curve of the main driving factor, i.e., GHI, is shown on the right axis to observe the lead and lag of the system performance. As can be seen, there is a time lag of about 1 h between the temperature difference and the radiation curve, indicating heat storage and thermal inertia. There is a good agreement between the results of mathematical modeling and the experimental data during daytime hours. Before sunrise, the mathematical model predicts a decrease in temperature difference, which can be justified due to the interruption of radiation. In contrast, the experimental data show an increase in the temperature difference. Other factors affecting the flow rate, such as turbine shutdown or closing the inlet gates at night, could be responsible for this difference in temporal performance. Also, a noticeable decrease in the temperature difference in the last hours of the day is probably related to the sudden changes in weather conditions, i.e., blowing ACW and mixing with air inside the collector. Such issues have been clearly explained in the validation of the modeling results of Hurtado et al. [13].

The chimney in this type of power plant acts like a heat engine and converts part of the heat energy absorbed in the collector into kinetic energy. The updraft velocity inside the chimney is considered an indicator of the kinetic energy produced in the system, where the simulation results are compared to the Manzanares prototype experimental data are shown in Fig. 5. The modeling results agree with the experimental results in a wide range of hours of the day. The sharp drop in updraft velocity around the sunset may be related to the unreported changes in the operational regime of the power plant, changes in weather conditions, and environmental crosswinds [13]. The velocity recovery in the hours after the radiation cut-off indicates a temporary change in the

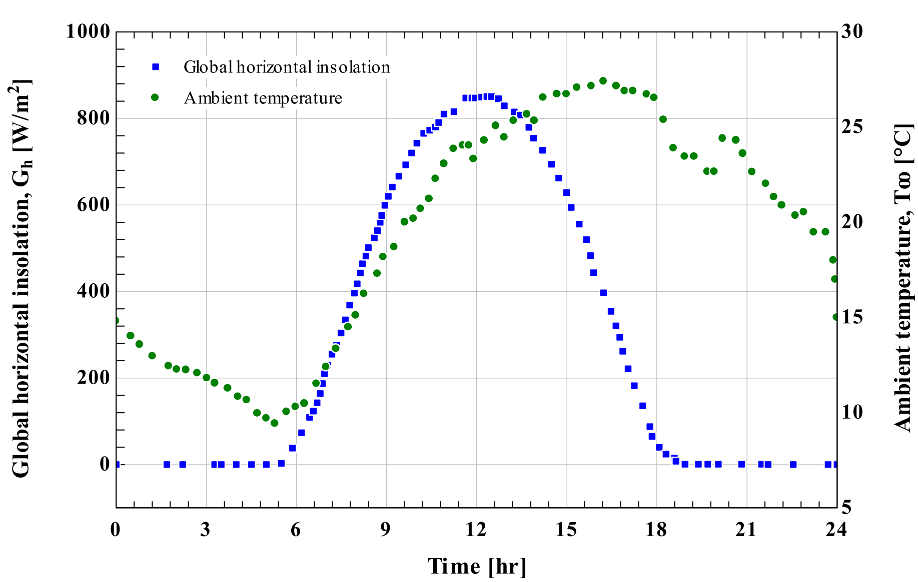

Fig. 3. Measured data of global horizontal insolation and ambient temperature of Manzanares power plant [5].

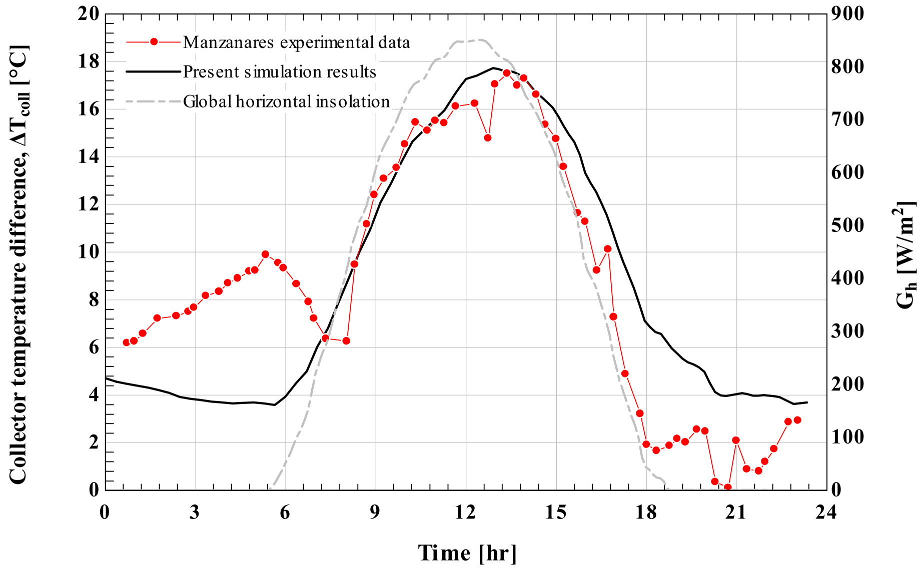

Fig. 4. Simulation results validation with the experimental data of Manzanares power plant [5] for the temperature difference in the solar collector.

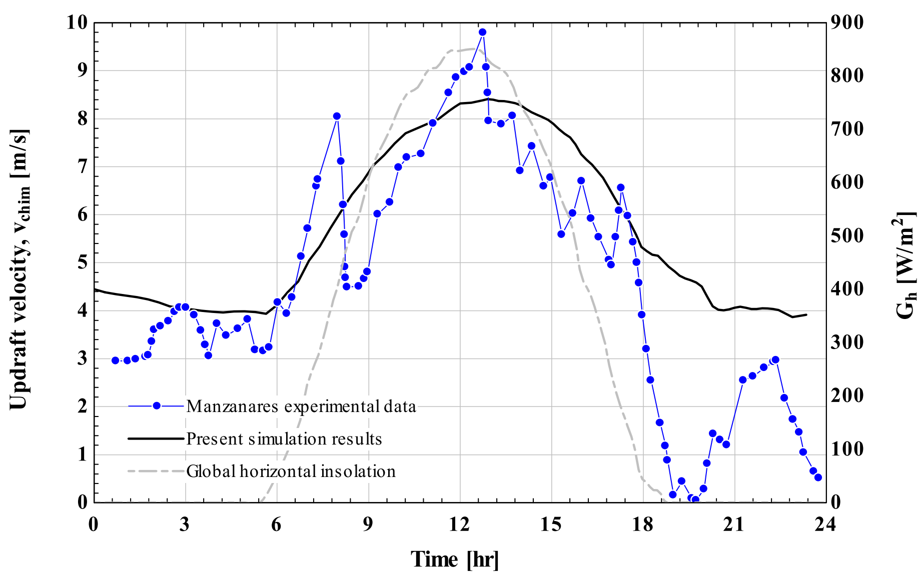

Fig. 5. Simulation results validation with the experimental data of Manzanares power plant [5] for the updraft velocity induced in the chimney.

operation of the power plant. Fig. 6 shows the experimental and simulated curves related to power generation. The experimental data have been reported only for daytime hours, indicating that the turbine was connected to a load for the same hours. There is a good agreement between the simulation results and the experimental data.

Fig. 7 shows the simulation result and their comparison with the experimental data for the ground surface and different depths of TES temperature. Besides an acceptable agreement between the experimental and simulation results, a time delay of about 1.5 h is observed in the thermal storage surface temperature compared to the solar radiation curve.

Due to the uncertainties in measured values of soil compaction, thermal conductivity, density, and heat capacity properties, some deviations are observed for TES temperatures at 10 and 50 cm depths. The time delay of the temperature response compared to the GHI curve increases with the increase in depth, and the temperature changes decrease due to the increase in thermal inertia. Temperature changes are practically insignificant for a depth of 0.5 m or more. Thermal penetration has been done up to this value, which is considered the effective depth of TES.

4.3. Effects of thermal energy storage on SCPP time-dependent performance

The TES system is the main component of an SCPP, which moderates power generation fluctuations caused by time changes in the main driving factor of solar radiation and enables continued power generation after the interruption of radiation and night hours. This section discusses a comparative analysis of the simulation results of an SCPP performance using various natural and artificial thermal storages. Manzanares power plant with limestone soil TES [5] has been chosen as the reference case, and the changes in other case studies have been highlighted.

4.3.1. TES materials

Different case studies in this research have been defined only based on changes in the thermophysical properties of TES material, comprising density, specific heat capacity, and thermal conductivity, compared to the Manzanares reported data [5]. Table 2 presents the types and

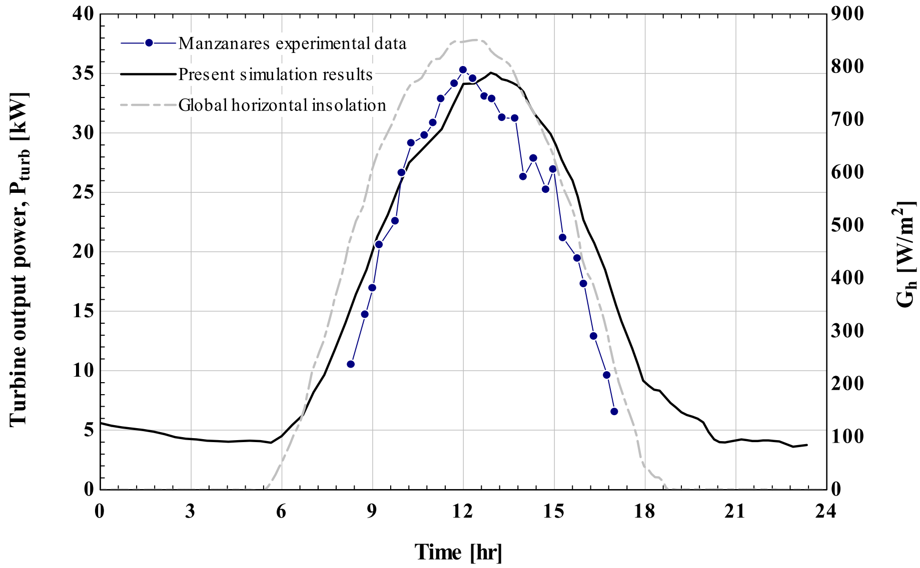

Fig. 6. Simulation results validation with the experimental data of Manzanares power plant [5] for the output power generation in aero-turbine.

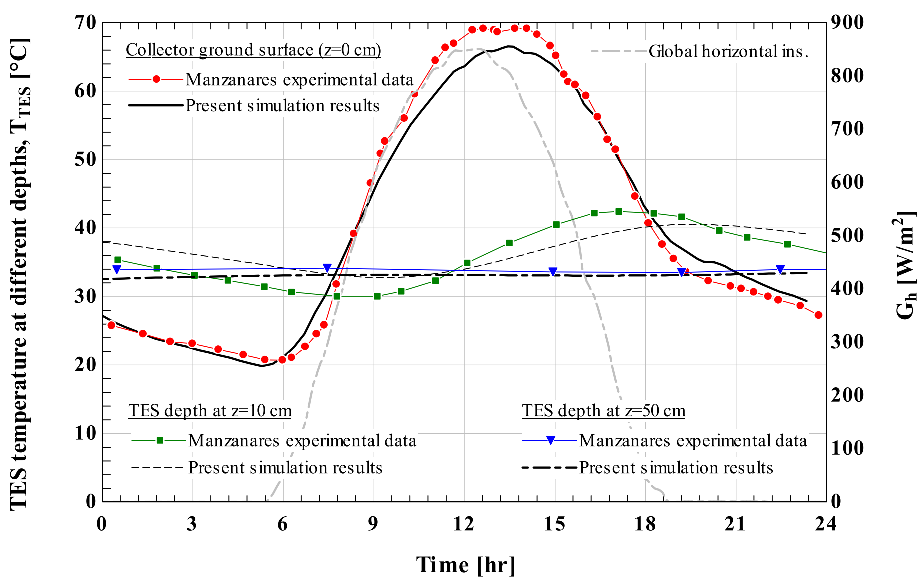

Fig. 7. Simulation results validation with the experimental data of Manzanares power plant [5] for the temperature of collector ground surface, TES depths z = 10 cm and z = 50 cm.

thermophysical properties of selected materials for thermal storage, whether natural or artificial. Some rare natural materials, such as quartz rock or marble stone, are only for comparison and will give indicators to evaluate the effect of other materials. Also, using some artificial materials should be considered from an environmental point of view and life cycle assessment. For example, the cement production process is associated with significant emissions of CO_2, which intensifies global warming.

In addition, thermal diffusivity and thermal effusivity or heat penetration coefficient [29] are reported based on equations (45) and (46), respectively.

$$\alpha_{TES} = \frac{k_{TES}}{\rho_{TES} c_{TES}} \tag{45}$$

$$b_{TES} = \sqrt{\rho_{TES} c_{TES} k_{TES}} \tag{46}$$

4.3.2. *Investigation of various TES materials on time-dependent performance parameters*

Performance simulation of the SCPP has been done for the fifteen cases defined in Table 2. The most common trend in all results is the increase in the decay of driving factors fluctuations in the intermediate and output variables of the system with an increase in the thermal effusivity of TES material.

Fig. 8 shows the temporal variation of the collector temperature difference as a factor in creating the natural convection in the plant. With the increase in thermal effusivity, the time delay of the curves has increased to a limited extent. Meanwhile, the amplitude of the fluctuations has been significantly reduced. The reference case, i.e., limestone soil [5], has a very close behavior to materials such as cement, brick, and asphalt because of similar thermal effusivities. The highest fluctuation is related to sand storage, with an 18.8 °C difference between the maximum and minimum values. The lowest fluctuation is observed for quartz storage, with the changes equal to 5.2 °C. Water-filled bags or tubes TES has been recommended by researchers [14,18,29,60,61,63],

Table 2
Thermophysical properties of various materials for thermal energy storage [7,34,59,64–66].

#	TES Material	ρ_{TES} [kg/m^3]	c_{TES} [J/kg-K]	k_{TES} [W/m-K]	α_{TES} [m^2/s]	b_{TES} [W-s$^{0.5}$/K-m^2]
0	Limestone soil[a] (Ref. case)	1900	840	0.75	4.699E-07	1094
1	Asphalt	2115	920	0.62	3.190E-07	1098
2	Brick	1920	835	0.72	4.490E-07	1074
3	Cement	1860	780	0.72	4.960E-07	1022
4	Clay	1460	880	1.30	1.012E-06	1292
5	Concrete	2300	880	1.40	6.920E-07	1683
6	Granite rock	2630	775	2.79	1.369E-06	2385
7	Limestone rock	2320	810	2.15	1.144E-06	2010
8	Marble rock	2680	830	2.80	1.259E-06	2496
9	Quartzite rock	2640	1105	5.38	1.844E-06	3962
10	Sandstone rock	2150	745	2.90	1.811E-06	2155
11	Sand	1515	800	0.27	2.230E-07	572
12	Soil (clay, sand, and silt)	2050	1840	0.52	1.380E-07	1401
13	Water (bags or tubes)	996	4179	0.61	1.470E-07	1597
14	Wet soil (in closed and dark-colored bags)	1900	2200	2.00	4.780E-07	2891

[a] The reference study of the Manzanares power plant is related to the experienced natural TES. According to Haaf et al. [7], the ground of the plant site was limestone soil with the properties listed in the table.

even the designer of the Manzanares prototype, Schlaich [4,6], due to its favorable thermal capacity and performance in various modeling studies. As shown in all figures, the effect of water TES is very similar to clay and soil materials. So, it cannot perform an expected role in improving thermal storage in an SCPP. It is worth mentioning that previous studies have often used a lumped body model for water TES, and the heat penetration and diffusion capacity have not been studied.

Fig. 9 shows the collector ground surface temperature for various TES materials. Heat storage surface is critical because of solar radiation absorption and convection heat transfer into flowing air. Compared to the reference case where the daily temperature variation has reached 46 °C, this performance parameter has increased by 11 °C for the sand storage and decreased by 19 °C for the wet soil TES. In the case of the water-filled bags or tubes, there is no significant difference compared to the clay and soil, especially during the hours of radiation interruption.

Evaluating a TES charging and discharging processes is one of the main aspects of studying time-dependent behavior. Fig. 10 shows the rate of conduction heat transfer at the TES boundary for different materials. Positive and negative values are related to the charging and discharging process. All the graphs are phase-lead compared to the radiation curve, and this phase advance increases with the decrease of thermal effusivity. The thermal power related to the storage discharge had almost constant values for the night hours. The quartz rock and wet soil storage have shown the highest charging/discharging capacity.

The effect of change in TES material on updraft velocity is shown in Fig. 11. Smooth curves with fewer changes have been obtained with increased thermal effusivity.

The difference between the maximum and minimum updraft velocity for the reference case is about 4.2 m/s. It increased to 6.1 m/s for sand storage and decreased to 2.2 m/s for wet soil. Also, the velocity curves in the hours of radiation interruption and night tend to be almost constant. For example, the wet soil storage has experienced changes of 0.5 m/s during the night hours, while the reference case has changed more than 1.5 m/s.

The temporal variation of output power is shown in Fig. 12. The difference between the maximum and minimum power generation has decreased by increasing thermal effusivity, and SCPP has been able to produce more power in the hours of radiation interruption.

The maximum time delay of power generation compared to solar radiation is about 2 h. Besides highly efficient stone/rock storage such as granite, marble, and quartz, the only competitive, available, and applicable option at the level of the requirements of the SCPP is wet soil thermal storage. This material has benefited from both the high density of soil and the high specific heat capacity of water. Due to the proximity

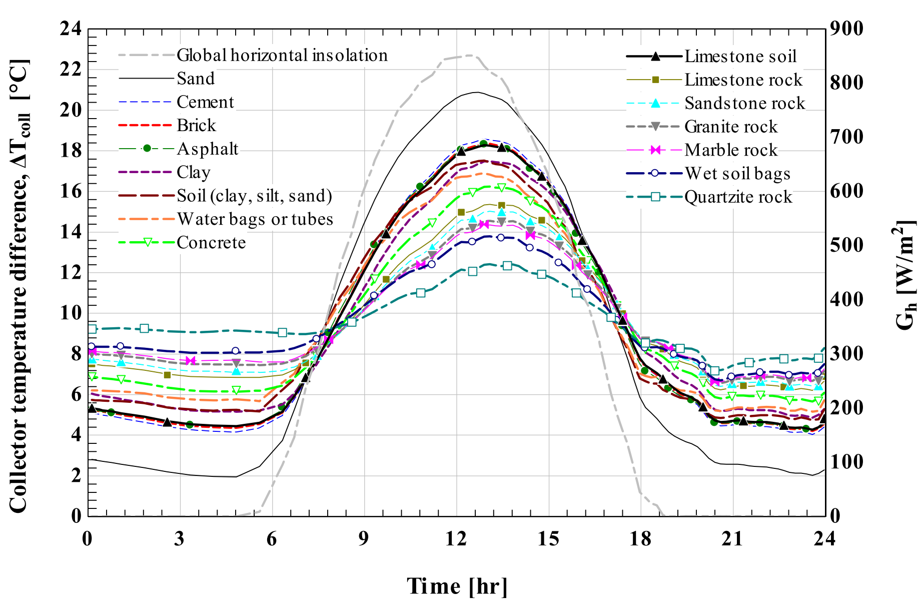

Fig. 8. Effect of TES material on time-dependent behavior of temperature difference created in the collector.

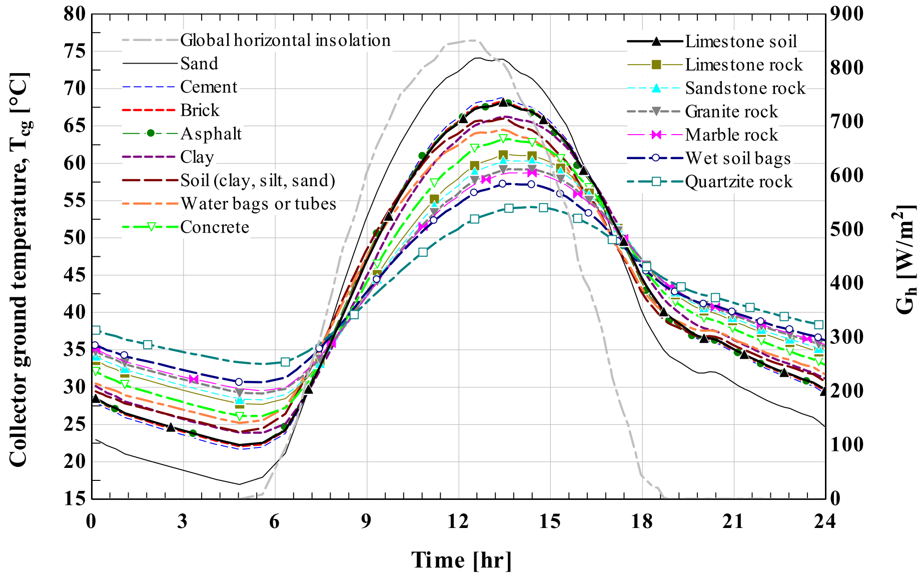

Fig. 9. Effect of TES material on time-dependent behavior of collector ground surface temperature.

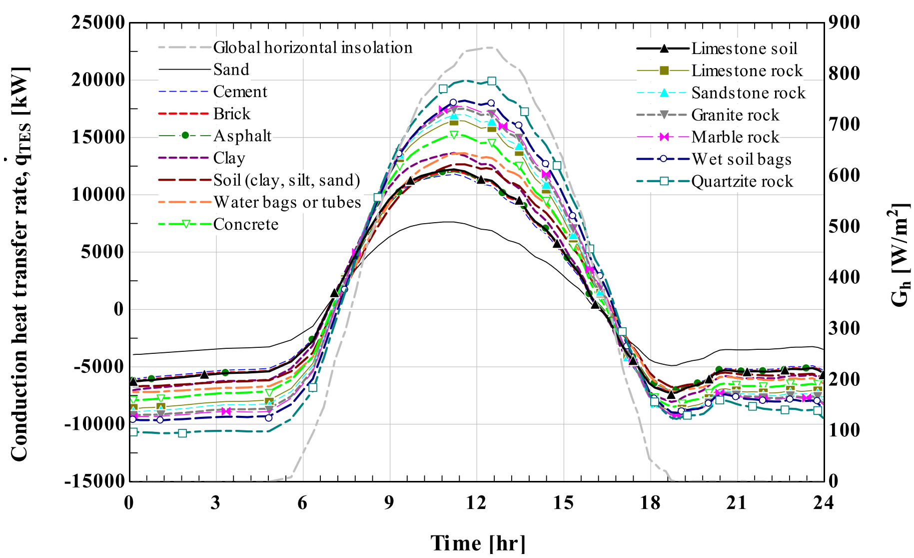

Fig. 10. Effect of TES material on time-dependent behavior of conduction heat transfer rate in TES.

of solid particles with liquid fluid, it has obtained significant thermal conductivity. It is important to highlight that the heat storage approach adopted in this study focuses specifically on single-phase sensible heat mode. Consequently, like the closed bags or tubes filled with water that previous researchers have extensively investigated, wet soil is employed within dark-colored, sealed bags.

4.3.3. Investigation of average and integral indicators of SCPP performance

The overall values and the temporal performance indicators have been evaluated in this subsection. According to Fig. 3, the average ambient temperature is equal to 19.45 °C, and the average GHI is calculated to be 277 W/m^2. The first integral index is the amount of generated electrical energy, defined according to equation (47). The average thermal efficiency [67] is expressed as equation (48).

$$E_{out} = \int_{day} P_{turb}\, dt \tag{47}$$

$$\overline{\eta}_{th} = \frac{E_{out}}{Q_{in}} = \frac{\int_{day} P_{turb}\, dt}{A_{coll} \int_{day} G_h\, dt} \tag{48}$$

The maximum thermal or Carnot efficiency of an SCPP is obtained, assuming no irreversibility in the system. It is calculated using the average ambient temperature and equation (49) [67]. The maximum thermal efficiency has a constant value equal to 0.6455 % for all the studied cases.

$$\overline{\eta}_{th,\max} = \frac{gH_{chim}}{c_p \overline{T}_\infty} \tag{49}$$

according to equation (50), the second law efficiency for an SCPP is the ratio of the actual thermal efficiency to the maximum thermal efficiency related to the reversible cycle [67]. This efficiency indicates how much maximum power can be produced in the actual operating conditions.

$$\overline{\eta}_{II} = \frac{\overline{\eta}_{th}}{\overline{\eta}_{th,\max}} \tag{50}$$

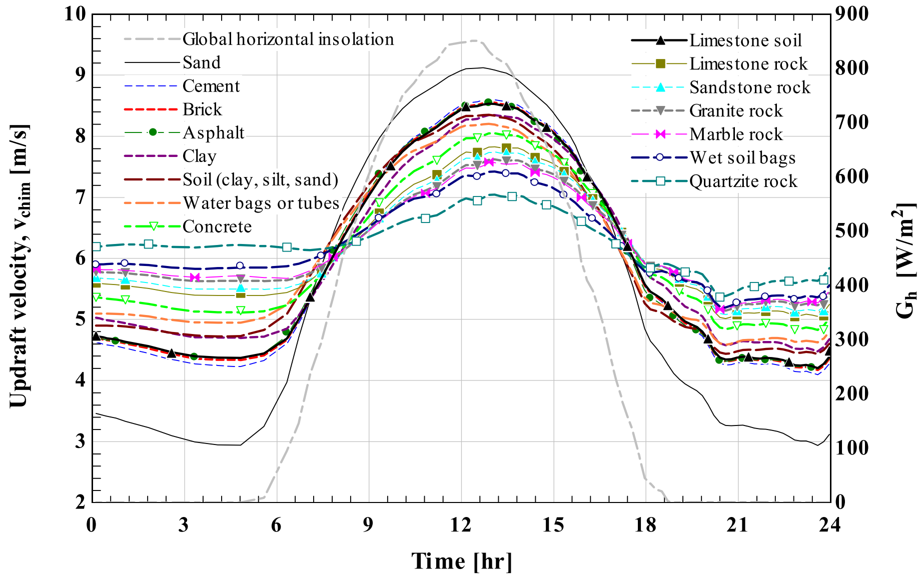

Fig. 11. Effect of TES material on time-dependent behavior of updraft velocity inside the chimney.

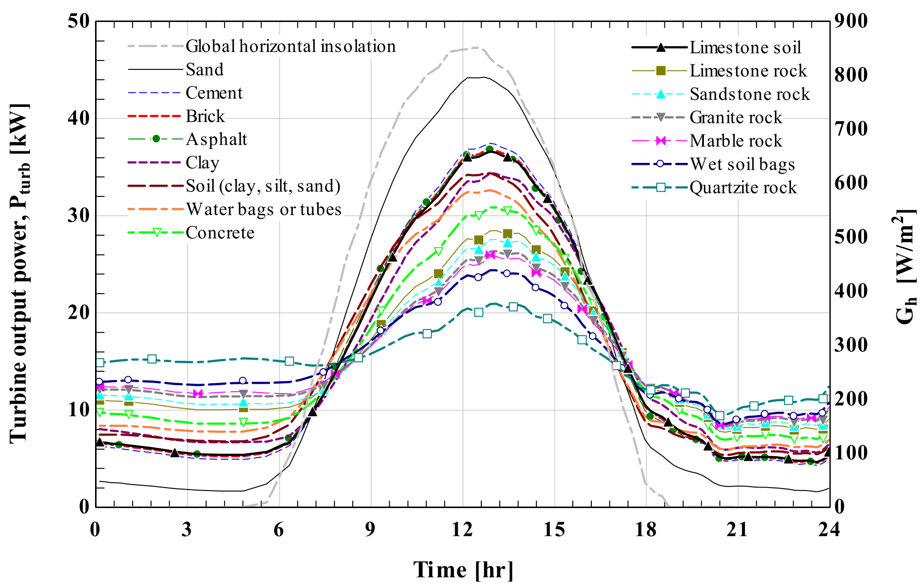

Fig. 12. Effect of TES material on time-dependent behavior of plant output power.

It is evident that the mentioned integral-based values do not provide information about the fluctuations and the level of changes in the integrant function. Capacity Factor (CF) is an index that quantifies the effects of power generation fluctuations and interruptions, defined in equation (51) [68].

$$CF = \frac{E_{out}}{P_{turb,\max}\int_{day} dt} \tag{51}$$

CF indicates the timeshare of the plant generation at its maximum or rated power concerning the entire operational period. A higher CF value means fewer time fluctuations and interruptions in power generation. The capacity factor does not provide further information about the amount of generated power. Based on equation (52), the Quality Factor of power generation (QF), defined as the product of average second law efficiency by the capacity factor, is a comprehensive index introduced in this research for the first time.

$$QF = \overline{\eta}_{II} \times CF \tag{52}$$

finally, the collector and storage efficiencies are expressed in equations (53) and (54), respectively.

$$\overline{\eta}_{coll} = \frac{Q_{ca}}{Q_{in}} = \frac{\int_{day} \dot{m} c_p \Delta T_{coll}\, dt}{A_{coll}\int_{day} G_h\, dt} \tag{53}$$

$$\overline{\eta}_{stor} = \frac{Q_{TES,charg\ e}}{Q_{in}} = \frac{\int_{day} \text{Heaviside}\left(\dot{q}''_{TES}\right)\dot{q}''_{TES}\, dt}{\int_{day} G_h\, dt} \tag{54}$$

The values of average and integral indicators for 15 desired case studies are reported in Table 3 in the order of increasing thermal effusivity. As can be seen, with the increase in thermal storage capacity, the thermal efficiency of the solar collector has not changed significantly. It has decreased with a gentle slope from 42.3 % for sand storage to 40.7 % for wet soil and quartz storage. At the same time, the storage efficiency has increased significantly and has grown by about 12 % (absolute) only from the reference case to the wet soil TES. These trends show that more solar radiation has been converted into heat used in the plant. It is worth

Table 3
Values of average and integral indices of performance parameters with the change of TES material.

TES Material/ b_{TES} [W-s$^{0.5}$/m^2-K]	$\bar{\eta}_{coll}$ [%]	$\bar{\eta}_{stor}$ [%]	E_{out} [kWh]	$P_{turb,\max}$ [kW]	$\bar{\eta}_{th}$ [%]	$\bar{\eta}_{II}$ [%]	CF [%]	QF [%]
Sand/572	42.34	15.73	370.00	44.30	0.1191	18.4508	34.80	6.42
Cement/1022	41.51	23.91	363.89	37.63	0.1171	18.1410	40.30	7.31
Brick/1074	41.46	24.48	363.61	37.00	0.1170	18.1255	40.95	7.42
Limestone soil (Ref. case)/1094	41.44	24.77	363.33	36.76	0.1169	18.1100	41.18	7.46
Asphalt/1098	41.46	24.35	363.61	36.80	0.1170	18.1255	41.17	7.46
Clay/1292	41.25	27.57	362.22	34.54	0.1165	18.0480	43.69	7.89
Soil (clay, sand, and silt)/1401	41.33	25.82	363.33	34.48	0.1169	18.1100	43.90	7.95
Water (bags or tubes)/1597	41.19	27.7	362.50	32.75	0.1166	18.0635	46.12	8.33
Concrete/1683	41.05	30.79	361.11	31.02	0.1162	18.0015	48.50	8.73
Limestone rock/2010	40.95	33.3	360.83	28.65	0.1161	17.9861	52.48	9.44
Sandstone rock/2155	40.92	34.3	360.56	27.75	0.1161	17.9861	54.14	9.74
Granite rock/2385	40.87	35.36	360.56	26.51	0.1160	17.9706	56.68	10.19
Marble rock/2496	40.85	35.83	360.56	25.97	0.1160	17.9706	57.85	10.40
Wet soil (bags or enclosure)/2891	40.72	36.93	359.72	24.55	0.1158	17.9396	61.07	10.95
Quartzite rock/3962	40.74	40.63	360.83	21.11	0.1161	17.9861	71.22	12.81

mentioning that with the increase in thermal effusivity, the heat converted from solar radiation will be at a lower working temperature. A low-temperature heat has lower availability to be converted into output power from the second law of thermodynamics point of view.

The energy generated in a daily cycle, the maximum power generation, and first and second-law efficiencies have decreased with the increase of the thermal effusivity of a TES. The changes in efficiency values are tiny, showing that TES does not significantly change the performance of converting thermal power into electrical power. The second-law efficiency has decreased by 0.2 % (absolute) from the reference case to the wet soil TES. The capacity factor has grown significantly from 41.18 % for the reference case to 61.07 % for wet soil thermal storage. The quality factor of power generation has increased with thermal effusivity. Regardless of the rare thermal storage of quartz rock, the wet soil TES has performed the best by a significant difference compared to others. The improvement obtained from water thermal storage is not comparable to other materials, especially wet soil.

According to Fig. 13, the wet soil TES has increased the QF from the reference value of 7.46 % up to 10.95 %, with a relative enhancement of 46.78 %.

4.3.4. Investigation of heat penetration depth in a TES and determination of effective depth

In addition to the amount of heat that can accumulate in a TES, the investigation of Heat Penetration Depth (HPD) is an important issue that should be considered from a technical and economic point of view, especially in using materials for artificial TES. Of course, in the case of natural heat storage, determining and evaluating the HPD will significantly affect the result of site locating for an SCPP. HPD is the depth after which the material forming the storage no longer experiences temperature fluctuations related to the absorption and dissipation of heat in daily operations. Fig. 14 shows the results related to reference thermal storage of Manzanares power plant, sandstone, quartz stone, and wet soil TES. The interval between successive curves is about 1 h and 20 min, and 19 curves have been plotted for the 24-h performance for each TES material. The HPD was about 0.5 m in daily operation for the reference case. The temperature distribution and HPD for asphalt, brick, and cement thermal storage were almost similar and consistent with the reference study results. The temperature distribution and HPD in rock/stone storage are observed to be relatively similar and independent of the thermal effusivity. The remarkable similarity of the temperature curves between the quartz stone and the sandstone storage, which have a hundred percent difference in thermal effusivity, shows that the

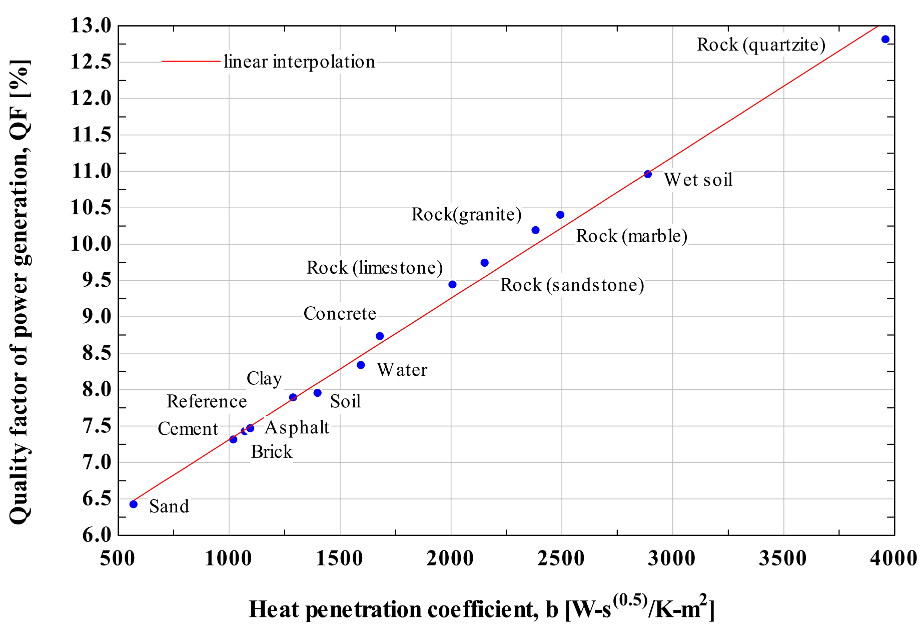

Fig. 13. Effect of the thermal effusivity of the TES material on the quality factor of power generation.

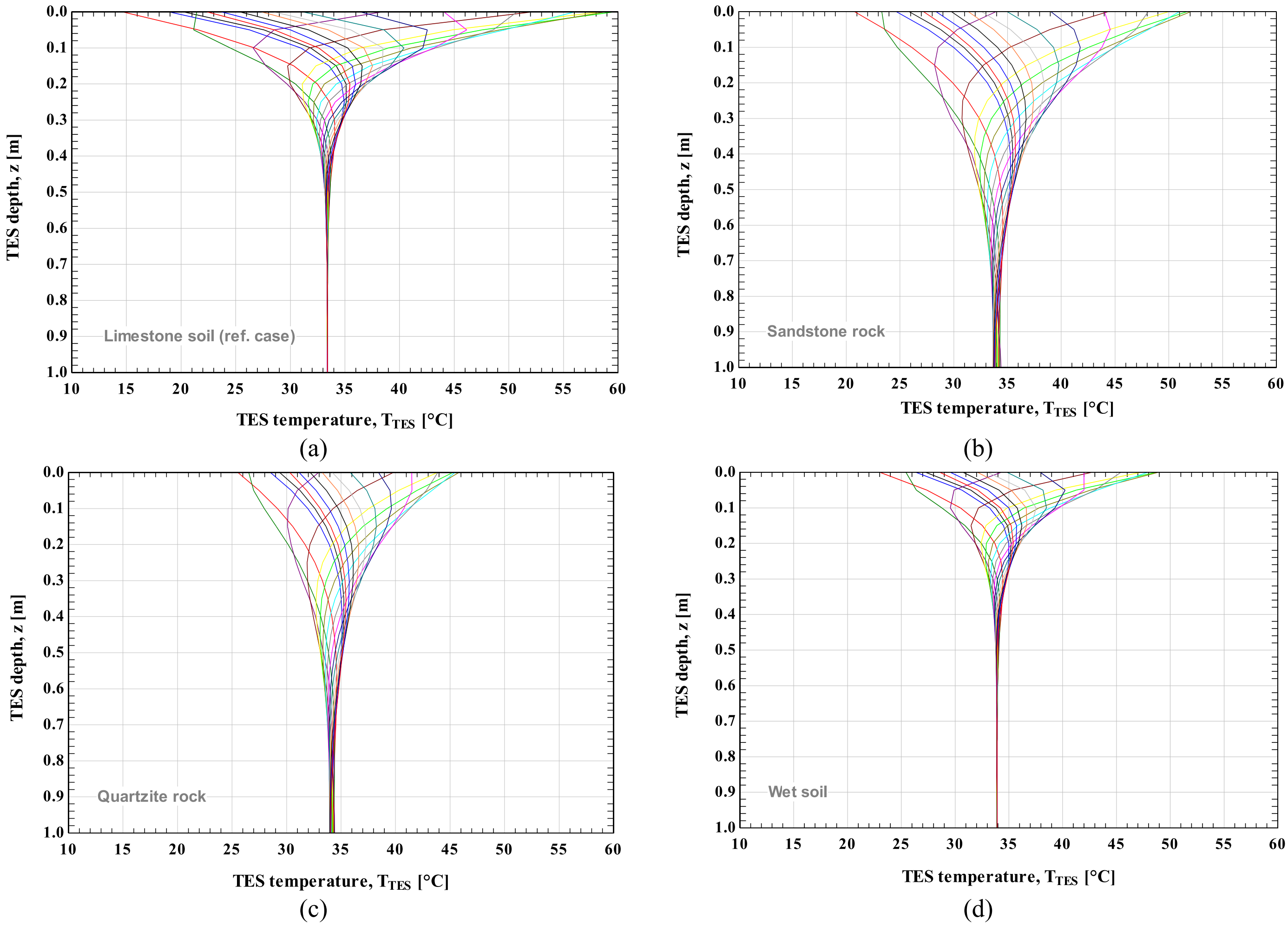

Fig. 14. Heat penetration depth in the daily operation of (a) reference (limestone soil), (b) sandstone rock, (c) quartzite rock, and (d) wet soil TES.

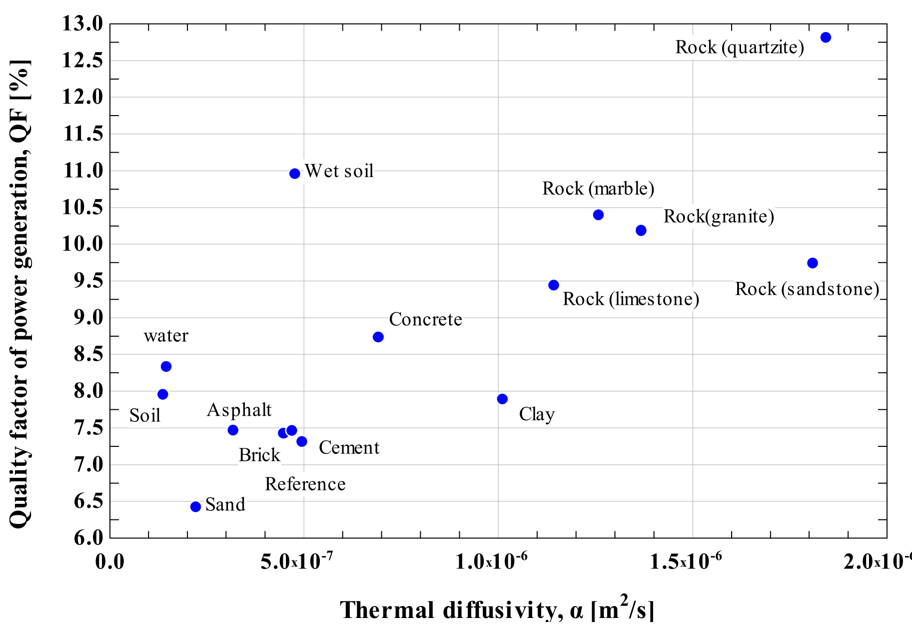

Fig. 15. Quality factor of power generation versus thermal diffusivity.

amount of heat storage capacity is not directly related to the depth of heat penetration in a TES.

Rearrangement of the analyzed items based on the thermal diffusivity shows that the HPD is an ascending function of this material property. The similarity of thermal diffusivity for sandstone and quartz rock in Table 2 justifies the similarity between the temperature distribution curves. Analytical solutions for transient conduction in a semi-infinite thick slab under simple harmonic excitation also show that HPD is proportional to the square root of thermal diffusivity [39]. Thus, optimal thermal storage has a constituent material with maximum thermal effusivity and minimum HPD or thermal diffusivity. A comparison of temperature distribution curves and HPD for soil and water-filled thermal storages showed a significant similarity. Their temperature changes and HPD range are about 40 °C and 0.4 m, respectively. On the other hand, the design, manufacturing, and operation of water-filled bags or tubes are more complex than soil storage.

According to Fig. 14, the heat penetration depth in wet soil TES is relatively low. The range of temperature changes is about 26 °C, and the HPD is about 0.5 m. As a material with the possibility of access and high abundance, the thermal storage of wet soil competes with rock or stone storage, especially quartz TES.

On the other hand, the HPD in stone TESs is, on average, twice that of wet soil TES, and a large volume of material is required to use them to achieve the expected thermal performance. As a result, besides its excellent heat storage capacity, wet soil TES is the optimal option concerning HPD and the required volume of material. In addition, the abundance of this material in nature and the possibility of easy and low-cost construction, preparation, and handling have created significant advantages compared to stone TES.

In order to have a better comparison, the quality factor of power generation is plotted versus the thermal diffusivity of different TES materials in Fig. 15. The lowest heat penetration depth is related to soil and water, with the quality factor of power generation of 7.95 % and 8.33 %, respectively. These two materials are close to each other regarding HPD and thermal storage capacity. Stone TES generally has a high QF, but they are not desirable due to their high thermal diffusivity and high HPDs. In comparison, wet soil has the highest QF and the lowest HPD simultaneously. This material is considered the optimal choice for thermal energy storage.

5. Conclusions and remarks

In the present work, a comprehensive mathematical model has been developed for predicting the time-dependent performance of an SCPP equipped with natural or artificial thermal energy storage. The model has been validated against the available experimental data of the Manzanares prototype for collector temperature difference, updraft velocity, TES layers temperature, and output power. The main highlights of this research are:

1 The effect of using various TES materials on the temporal performance parameters of the SCPP has been analyzed and compared against the reference material.
2 Simulation results reveal no considerable difference between water-filled bags or tubes TES and other materials such as clay and soil.
3 Among the different materials, sand exhibits the highest fluctuation, with a notable temperature difference of 18.8 °C between the maximum and minimum values. On the other hand, quartz storage demonstrates the lowest fluctuation, with temperature changes amounting to only 5.2 °C. Overall, rocky/stone TESs show better performance in mitigating fluctuations and interruptions. However, the practical feasibility of utilizing quartz or marble stone TESs is limited.
4 Despite the increase in thermal storage capacity, the thermal efficiency of the solar collector has not shown significant changes. Instead, it has experienced a slight decrease with a gradual decline. For instance, the thermal efficiency has decreased from 42.3 % in the case of sand storage to 40.7 % for both wet soil and quartz storage.
5 The studied type of wet soil, i.e., the specific wet mixture of clay, sand, and silt in closed and dark-colored bags, has been highlighted as an optimal TES, which benefited from both the high density of soil and the high specific heat capacity of water as well as considerable thermal conductivity due to the proximity of solid particles with liquid fluid.
6 It is observed that the capacity to moderate fluctuations and interruptions directly depends on the thermal effusivity or heat penetration coefficient of TES material.
7 Investigation of average and integral indicators shows that TES enhancement slightly reduces the average output power but significantly affects the plant capacity factor. The capacity factor has grown from 41.18 % for the limestone soil to 61.07 % for wet soil thermal storage.
8 The quality factor of power generation, which is introduced in this research, enhanced from 7.46 % for the reference Manzanares TES, i.e., limestone soil, to 10.95 % for wet soil, while the water TES is shown to enhance the QF to reach 8.33 %.
9 The temperature distributions in a TES for daily operation show that the heat penetration depth is directly related to thermal diffusivity. Rocky/stone TESs have high HPD values, while wet soil TES requires a lower HPD for the same thermal performance. Specifically, wet soil TES demonstrates an HPD of 0.5 m.

CRediT authorship contribution statement

Amir Arefian: Methodology, Data curation, Writing – original draft. **Reza Hosseini-Abardeh:** Conceptualization, Investigation, Supervision. **Mohsen Rahimi-Larki:** Methodology, Formal analysis, Writing – review & editing. **Arman Torkfar:** Software, Validation, Writing – review & editing. **Hamid Sarlak:** Supervision, Resources, Project administration.

Declaration of competing interest

The authors declare that they have no known competing financial interests or personal relationships that could have appeared to influence the work reported in this paper.

Data availability

Data will be made available on request.

References

[1] Sheikh MRI. Energy storage. BoD–Books on Demand; 2010.
[2] Ter-Gazarian AG. Energy storage for power systems. second ed., vol. 6. Iet): The Institution of Engineering and Technology; 2010.
[3] Chikere AO, Al-Kayiem HH, Karim ZAA. Review on the enhancement techniques and introduction of an alternate enhancement technique of solar chimney power plant. J Appl Sci 2011;11(11):1877–84. https://doi.org/10.3923/jas.2011.1877.1884.
[4] Schlaich Jr, Bergermann R, Schiel W, Weinrebe G. Design of commercial solar updraft tower systems—utilization of solar induced convective flows for power generation. J Sol Energy Eng 2005;127(1):117. https://doi.org/10.1115/1.1823493.
[5] Haaf W. Solar chimneys: part ii: preliminary test results from the Manzanares pilot plant. Int J Sustain Energy 1984;2(2):141–61. https://doi.org/10.1080/01425918408909921.
[6] Schlaich J, Robinson M, Schubert FW. The solar chimney: electricity from the sun. Germany: Axel Menges Geislingen; 1995.
[7] Haaf W, Friedrich K, Mayr G, Schlaich J. Solar chimneys part I: principle and construction of the pilot plant in Manzanares. Int J Sol Energy 1983;2(1):3–20. https://doi.org/10.1080/01425918308909911.
[8] Zhou X, Yang J, Xiao B, Hou G. Experimental study of temperature field in a solar chimney power setup. Appl Therm Eng 2007;27(11–12):2044–50. https://doi.org/10.1016/j.applthermaleng.2006.12.007.
[9] Mamgain S, Aggarwal S, Sharma M, Shukla AK. "Recent perspectives and outlook of advances in technologies of solar chimney power plant," in Journal of Physics: conference Series. IOP Publishing 2022;2178(1):012009.

[10] Fanlong M, Tingzhen M, Yuan P. "A method of decreasing power output fluctuation of solar chimney power generating systems," in 2011 third international conference on measuring technology and mechatronics automation, Shanghai, China, vol. 1. IEEE; 2011. p. 114–8. https://doi.org/10.1109/ICMTMA.2011.34.
[11] Chaichan MT, Kazem HA. Thermal storage comparison for variable basement kinds of a solar chimney prototype in baghdad - Iraq weathers. Int J Appl Sci 2011;2(2): 12–20.
[12] Ming T, Meng F, Liu W, Pan Y, Kiesgen de Richter R. Analysis of output power smoothing method of the solar chimney power generating system. Int J Energy Res 2012;37(13):1657–68. https://doi.org/10.1002/er.2986.
[13] Hurtado FJ, Kaiser AS, Zamora B. Evaluation of the influence of soil thermal inertia on the performance of a solar chimney power plant. Energy 2012;47(1):213–24. https://doi.org/10.1016/j.energy.2012.09.040.
[14] dos Santos Bernardes MA, Zhou X. On the heat storage in Solar Updraft Tower collectors–Water bags. Sol Energy 2013;91:22–31. https://doi.org/10.1016/j.solener.2012.11.025.
[15] Bernardes MAdS. On the heat storage in Solar Updraft Tower collectors – influence of soil thermal properties. Sol Energy 2013/12/01/2013;98:49–57. https://doi.org/10.1016/j.solener.2013.07.014.
[16] Larbi S, Bouhdjar A, Meliani K, Taghourt A, Semai H. Solar chimney power plant with heat storage system performance analysis in South Region of Algeria. In: 2015 3rd international renewable and sustainable energy conference (IRSEC), Marrakech & Ouarzazate, Morocco. IEEE; 2015. p. 1–6. https://doi.org/10.1109/IRSEC.2015.7454948.
[17] Li J, Guo H, Huang S. Power generation quality analysis and geometric optimization for solar chimney power plants. Sol Energy 2016;139:228–37. https://doi.org/10.1016/j.solener.2016.09.033.
[18] Choi YJ, Kam DH, Park YW, Jeong YH. Development of analytical model for solar chimney power plant with and without water storage system. Energy 2016;112: 200–7. https://doi.org/10.1016/j.energy.2016.06.023.
[19] Bashirnezhad K, kavyanpoor M, Kebriyaee SA, Moosavi A. The experimental appraisement of the effect of energy storage on the performance of solar chimney using phase change material. Sol Energy 2018;169:411–23. https://doi.org/10.1016/j.solener.2018.05.001.
[20] Yaswanthkumar A, Chandramohan V. Numerical analysis of flow parameters on solar updraft tower (SUT) with and without thermal energy storage (TES) system. J Therm Anal Calorim 2019;136(1):331–43. https://doi.org/10.1007/s10973-018-7756-z.
[21] Amudam Y, Chandramohan V. Influence of thermal energy storage system on flow and performance parameters of solar updraft tower power plant: a three dimensional numerical analysis. J Clean Prod 2019;207:136–52. https://doi.org/10.1016/j.jclepro.2018.09.248.
[22] Sedighi AA, Deldoost Z, Karambasti BM. Effect of thermal energy storage layer porosity on performance of solar chimney power plant considering turbine pressure drop. Energy 2020;194. https://doi.org/10.1016/j.energy.2019.116859.
[23] Maia CB, Castro Silva JdO. Thermodynamic assessment of a small-scale solar chimney. Renew Energy 2022/03/01/2022;186:35–50. https://doi.org/10.1016/j.renene.2021.12.128.
[24] Ikhlef K, Larbi S, Üçgül İ. Experimental study of different thermal storage system effects on the performance of a small prototype solar chimney power plant. Renew Energy 2022/11/01/2022;200:516–26. https://doi.org/10.1016/j.renene.2022.09.087.
[25] Cuce E, et al. Performance assessment of solar chimney power plants with natural thermal energy storage materials on ground: CFD analysis with experimental validation. Int J Low Carbon Technol 2022. https://doi.org/10.1093/ijlct/ctac001.
[26] Méndez C, Bicer Y. Comparison of the influence of solid and phase change materials as a thermal storage medium on the performance of a solar chimney. Energy Sci Eng 2021. https://doi.org/10.1002/ese3.892.
[27] Guo P, Wang Y, Li J, Wang Y. Thermodynamic analysis of a solar chimney power plant system with soil heat storage. Appl Therm Eng 2016/05/05/2016;100: 1076–84. https://doi.org/10.1016/j.applthermaleng.2016.03.008.
[28] Howell JR, Menguc MP, Siegel R. Thermal radiation heat transfer. sixth ed. CRC press; 2016.
[29] Zhou X, Xu Y. Solar updraft tower power generation. Sol Energy 2016;128:95–125. https://doi.org/10.1016/j.solener.2014.06.029.
[30] Ong KS, Chow CC. Performance of a solar chimney. Sol Energy 2003;74(1):1–17. https://doi.org/10.1016/s0038-092x(03)00114-2.
[31] Aurélio dos Santos Bernardes M, Von Backström TW, Kröger DG. Analysis of some available heat transfer coefficients applicable to solar chimney power plant collectors. Sol Energy 2009;83(2):264–75. https://doi.org/10.1016/j.solener.2008.07.019.
[32] Bernardes MADS. Convective heat transfer analysis of solar chimney power plant collectors. In: Belmiloudi A, editor. Heat transfer - mathematical modelling, numerical methods and information technology. InTech; 2011.
[33] M. S. Bhatti and R. K. Shah, Turbulent and transition flow convective heat transfer in ducts, in Handbook of Single-Phase Convective Heat Transfer, S. Kakaç, R. K. Shah, and W. Aung Eds., 1st ed.: Wiley-Interscience, 1987.
[34] Pretorius JP. "Optimization and control of a large-scale solar chimney power plant," PhD. Stellenbosch: Mechanical Engineering University of Stellenbosch; 2007.
[35] Bernardes MA dos S, Voß A, Weinrebe G. Thermal and technical analyses of solar chimneys. Sol Energy 2003;75(6):511–24. https://doi.org/10.1016/j.solener.2003.09.012.
[36] Yunus AC. Fluid mechanics: fundamentals and applications (si units). Tata McGraw Hill Education Private Limited; 2010.
[37] Hammadi SH. Solar updraft tower power plant with thermal storage. Basrah J Eng Res 2009;9(1):9–16.
[38] Li J, Guo H, Cheng Q, Huang S. Optimal turbine pressure drop for solar chimney-aided dry cooling system in coal-fired power plants. Energy Convers Manag 2017; 133:87–96. https://doi.org/10.1016/j.enconman.2016.11.063.
[39] Hahn DW, Özisik MN. Heat conduction. John Wiley & Sons; 2012.
[40] Kakaç S, Yener Y, Naveira-Cotta CP. Heat conduction. CRC Press; 2018.
[41] Koonsrisuk A, Chitsomboon T. Mathematical modeling of solar chimney power plants. Energy 2013;51:314–22. https://doi.org/10.1016/j.energy.2012.10.038.
[42] Von Backström T, Gannon A. The solar chimney air standard thermodynamic cycle. South African Inst Mech Eng, R & D J 2000;16(1):16–24.
[43] Zhou X, Yang J, Xiao B, Hou G, Xing F. Analysis of chimney height for solar chimney power plant. Appl Therm Eng 2009;29(1):178–85. https://doi.org/10.1016/j.applthermaleng.2008.02.014.
[44] White FM. Fluid mechanics, WCB. fourth ed. Boston: McGraw-Hill; 1999.
[45] Zhou X, Xu Y. Pressure losses in solar chimney power plant. J Sol Energy Eng 2018; 140(2). https://doi.org/10.1115/1.4038962.
[46] Ming T, Gong T, de Richter RK, Wu Y, Liu W. A moist air condensing device for sustainable energy production and water generation. Energy Convers Manag 2017; 138:638–50. https://doi.org/10.1016/j.enconman.2017.02.012.
[47] Guo P-h, Li J-y, Wang Y. Annual performance analysis of the solar chimney power plant in Sinkiang, China. Energy Convers Manag 2014;87:392–9. https://doi.org/10.1016/j.enconman.2014.07.046.
[48] Zhou X, Xu Y, Hou Y. Effect of flow area to fluid power and turbine pressure drop factor of solar chimney power plants. J Sol Energy Eng 2017;139(4). https://doi.org/10.1115/1.4036774.
[49] Guo P, Li J, Wang Y, Wang Y. Evaluation of the optimal turbine pressure drop ratio for a solar chimney power plant. Energy Convers Manag 2016;108:14–22. https://doi.org/10.1016/j.enconman.2015.10.076.
[50] Guo P, Li J, Wang Y, Liu Y. Numerical analysis of the optimal turbine pressure drop ratio in a solar chimney power plant. Sol Energy 2013;98:42–8. https://doi.org/10.1016/j.solener.2013.03.030.
[51] Zhou X, Wang F, Ochieng RM. A review of solar chimney power technology. Renew Sustain Energy Rev 2010;14(8):2315–38. https://doi.org/10.1016/j.rser.2010.04.018.
[52] Fluri TP, Von Backström TW. Performance analysis of the power conversion unit of a solar chimney power plant. Sol Energy 2008;82(11):999–1008. https://doi.org/10.1016/j.solener.2008.05.001.
[53] RahimiLarki M, Abardeh RH, Rahimzadeh H, Sarlak H. Performance analysis of a laboratory-scale tilted solar chimney system exposed to ambient crosswind. Renew Energy 2021;164:1156–70. https://doi.org/10.1016/j.renene.2020.10.118.
[54] Larkia MR, Arefian A, Abardeh RH. Experimental and numerical analysis of ambient crosswind effects on a floating solar chimney power plant performance. J Sol Energy Res 2016;1(2):40–6 [Online]. Available: https://jser.ut.ac.ir/article_62299_13605cfa3cd16254e93ae3fa055c4187.pdf.
[55] Arefian A, Hosseini Abardeh R. Ambient crosswind effect on the first integrated pilot of a floating solar chimney power plant: experimental and numerical approach. J Therm Anal Calorim 2021/02/25 2021. https://doi.org/10.1007/s10973-021-10620-w.
[56] Zhou X, Bernardes MAdS, Ochieng RM. Influence of atmospheric cross flow on solar updraft tower inflow. Energy 2012;42(1):393–400. https://doi.org/10.1016/j.energy.2012.03.037.
[57] Jaluria EAP, Pletcher Richard H, Anderson Dale A, Tannehill John C. Computational fluid mechanics and heat transfer. In: (Series in computational and physical processes in mechanics and thermal sciences). 3 ed. CRC Press; 2012.
[58] Klein S. Engineering equation solver (EES) for microsoft windows operating system: commercial and professional versions. Madison, WI: F-Chart Software; 2002.
[59] Klein S, Nellis G. Mastering EES. f-Chart software; 2012.
[60] Al-Kayiem HH, Aja OC. Historic and recent progress in solar chimney power plant enhancing technologies. Renew Sustain Energy Rev 2016;58:1269–92. https://doi.org/10.1016/j.rser.2015.12.331.
[61] Dhahri A, Omri A. A review of solar chimney power generation technology. Int J Eng Adv Technol 2013;2(3):1–17.
[62] Ngala GM, Sulaiman AT, Garba I. Review of solar chimney power technology and its potentials in semi-arid region of Nigeria. International Journal of Modern Engineering Research (IJMER) 2013;3(3):1283–9.
[63] Kasaeian AB, Molana S, Rahmani K, Wen D. A review on solar chimney systems. Renew Sustain Energy Rev 2017;67:954–87. https://doi.org/10.1016/j.rser.2016.09.081.
[64] Hamdhan IN, Clarke BG. Determination of thermal conductivity of coarse and fine sand soils. In: Proceedings of world geothermal congress; 2010. p. 1–7.
[65] Choi H, Mills A. Heat and mass transfer in metal hydride beds for heat pump applications. Int J Heat Mass Tran 1990;33(6):1281–8. https://doi.org/10.1016/0017-9310(90)90257-U.
[66] Incropera FP. Fundamentals of heat and mass transfer. sixth ed. Wiley India Pvt. Limited; 2010.
[67] Struchtrup H. Thermodynamics and energy conversion. Springer; 2014.
[68] Papageorgiou C. Floating solar chimney technology. Solar Energy" book of "INTECH" edited by Radu D. Rugescu 2010:187–222.